Research Square

Preprints are preliminary reports that have not undergone peer review.
They should not be considered conclusive, used to inform clinical practice,
or referenced by the media as validated information.

Atomic Readout of Kerr Nonlinearity and Loss UsingTwo Three-Level Atoms in an Optomechanical Cavity

Syed Jamal Anwar

sjamalanwar@gmail.com

Quaid-i-Azam University

S. Abdul Khalek S. Abdul Khalek

Taif University

Research Article

Keywords: cavity optomechanics, two three-level atoms, Kerr nonlinearity, quantum Fisher information, thermal mechanics, cavity loss, nuisance parameters

Posted Date: November 23rd, 2026

DOI: https://doi.org/10.21203/rs.3.rs-11734415/v1

License: This work is licensed under a Creative Commons Attribution 4.0 International License.
Read Full License

Additional Declarations: No competing interests reported.

Atomic Readout of Kerr Nonlinearity and Loss Using Two Three-Level Atoms in an Optomechanical Cavity

S. Jamal Anwar[1,*] and S. Abdul Khalek[2]

[1]Department of Physics, Quaid-i-Azam University, Islamabad 45320, Pakistan

[2]Department of Mathematics and Statistics, College of Science, Taif University, P.O. Box 11099, Taif 21944, Saudi Arabia

*Correspondence: sjamalanwar@gmail.com

November 2026

Abstract

We investigate estimation of intrinsic Kerr nonlinearity and photon loss using two cascade-type three-level atoms in a radiation-pressure optomechanical cavity. The two atoms begin in their ground states, the cavity in a two-photon Fock state, and the mechanical oscillator in a thermal state; these subsystems are initially uncorrelated. An unconditional local-bath master equation includes cavity leakage, independent atomic relaxation, and mechanical damping and heating, without linearizing the photon–phonon interaction. Conservation of total atom–field excitations under the coherent dynamics, together with excitation loss, restricts the atom–field register to ten states; the mechanical Fock cutoff is tested separately for convergence. Exact parameter derivatives distinguish atomic quantum Fisher information from information retained in the cavity and mechanics. At the chosen operating point, a calibrated dimensionless optomechanical coupling of 0.35 lowers the atomic Kerr information with unknown loss from 2.58180 to 1.93553 at dimensionless interaction time 3.2; atomic populations retain 1.57504. Increasing the assumed mechanical thermal occupation from zero to 0.5 lowers the corresponding information from 2.08922 to 1.43981 under the stated bath model. Treating optomechanical coupling as an additional unknown reduces the atomic benchmark further to 1.69318. An exact square-completion identity explains the mechanically induced Kerr shift, but a static shifted-Kerr surrogate does not reproduce the full reduced-state dynamics. The zero-time QFI and the absence of intrinsic-Kerr sensitivity with at most one excitation remain exact. Previously established zero-coupling benchmarks are retained explicitly as controls, including norm-matched qutrit–qubit comparisons and simulated population inference. The results quantify information transfer, thermal deterioration, and calibration costs in a few-photon hybrid sensor without claiming a universal mechanical enhancement.

Keywords: cavity optomechanics; two three-level atoms; Kerr nonlinearity; quantum Fisher information; thermal mechanics; cavity loss; nuisance parameters.

1 Introduction

Characterizing a nonlinear optical environment through embedded matter probes is useful when the intracavity field is difficult to measure directly or when the final detector naturally resolves atomic populations. The desired parameters then enter the field dynamics, while the experimental outcomes belong to a different subsystem. A large quantum Fisher information (QFI) for the combined atom–field state does not establish that the same precision is available from the atoms. Quantum statistical geometry supplies the relevant language: state distinguishability is bounded by

the QFI, but attainable precision also depends on the measured subsystem and the measurement itself [1–3]. Channel-identification theory further emphasizes that a physically specified input and an explicit readout are essential parts of an estimation problem [4].

Noisy quantum metrology treats sensitivity together with realistic loss and finite resources. General bounds show why ideal sensitivity alone can give a misleading account of a device's performance [5, 6]. This issue is particularly relevant to cavity quantum electrodynamics, where coherent excitation exchange can move information between matter and radiation before uncontrolled photons leave the system. Even when the complete dynamics is Markovian, subsystem information can rise and fall during this transfer. Such oscillations require an analysis of the encoding and reduction maps; their presence by itself does not establish environmental memory [7].

Three-level atoms offer an additional transition pathway and a larger measurement space than two-level atoms. Their atom–field dynamics have been investigated through entanglement, quantum statistics, squeezing, atomic motion, Stark shifts, and intrinsic decoherence [8–13]. Two three-level atoms interacting nonlinearly with a field have also been treated through effective two-level Hamiltonians obtained by eliminating an intermediate level [14]. Cavity-assisted generation of entangled three-level atomic states provides a complementary motivation for retaining the full ladder [15]. For an estimation task, however, retaining another level is useful only if it changes accessible parameter distinguishability under a stated resource comparison. Its mere presence in the Hilbert space is insufficient evidence of an advantage.

The Kerr interaction is attractive because it produces photon-number-dependent energy shifts and phases. Early work on nonlinear quantum optical dynamics and amplitude dispersion established a broad theoretical background [16, 17]. Observation of single-photon Kerr collapse and revival, together with deterministic preparation of large bosonic superpositions, demonstrates that nonlinear oscillator dynamics can be controlled experimentally [18, 19]. In a few-photon setting, the form of the nonlinear term is particularly consequential. The ordinary normally ordered interaction is proportional to $n(n-1)$, and its action vanishes on zero- and one-photon occupations. Models written instead with n^2 include an additional linear frequency shift. An estimation claim therefore has to state both its Kerr convention and the excitation support available during the interaction.

Existing nonlinear metrology already addresses important parts of this problem. Optimal estimation of bosonic loss clarifies the roles of probe statistics and readout [20]. Rossi, Albarelli, and Paris showed that Kerr nonlinearity can improve loss estimation in certain bosonic-channel regimes [21]. Asjad, Teklu, and Paris investigated joint loss and Kerr estimation in a driven resonator and analyzed quadrature detection [22]. Notarnicola, Olivares, and Paris subsequently studied noisy Kerr channels, including the incompatibility of simultaneous estimation [23]. Critical parametric sensing provides another route to nonlinear-cavity sensitivity [24]. These precedents establish that joint Kerr–loss estimation is already an active research problem; the present study concerns information accessible through two multilevel matter probes and a controlled few-photon comparison.

Atomic readout of Kerr parameters also has a direct precedent. Zidan, Abdel-Hameed, and Metwally calculated reduced-atomic QFI for two two-level atoms in a Kerr medium with intrinsic phase decoherence [25]. Earlier studies of two three-level atoms examined the influence of Kerr and Stark terms on QFI and entanglement dynamics [8]. The distinction investigated here is not the general possibility of atomic Kerr sensing. We jointly differentiate a full photon-loss master equation with respect to Kerr strength and cavity leakage, treat the leakage as an unknown nuisance in Kerr precision, retain both atomic transitions, and compare experimentally specified population readout with quantum bounds. Ground-state atoms and an initial two-photon Fock state make the available nonlinear pathway and the photon resource explicit.

A mechanical boundary adds a second nonlinear pathway. In cavity optomechanics, photon

number exerts a radiation-pressure force and the resulting displacement changes the cavity resonance [26]. Few-photon optomechanics can produce effective photon–photon interactions and photon blockade [27]. The relationship between an optomechanical resonator and a Kerr medium has been established in specified regimes, with mechanical fluctuations limiting a simple equivalence [28]. Nonlinear optomechanical quantum estimation has also been developed for light–matter coupling, mechanical forces, and squeezing [29]. These precedents motivate treating mechanics as a dynamical subsystem rather than replacing it at the outset by a static Kerr coefficient. In the present transient atomic-readout protocol, both the cavity and the mechanics are discarded before detection. Mechanical correlations may therefore alter the encoded response while keeping part of the parameter information inaccessible to the atomic detector.

More directly, Montenegro and collaborators analyzed estimation of atom–light and light–mechanics couplings with access to individual hybrid subsystems [30]. Atomic QFI in an optomechanical cavity has also been investigated for a diamond-type four-level atom [31]. These are direct precedents for restricted-access hybrid metrology. Here the target is intrinsic Kerr strength, with cavity loss and optionally radiation-pressure coupling as unknown nuisance parameters, under the stated two-atom preparation and unconditional dynamics.

Multiparameter quantum estimation introduces a further distinction between sensitivity and compatibility. Pure-state estimation, SLD compatibility conditions, and general treatments of several parameters show that separate optimal measurements need not be jointly implementable [32–34]. Numerical evaluation of the Holevo bound and tight bounds for incompatible parameters sharpen this limitation [35–37]. The normalized mean SLD commutator provides a useful diagnostic of this quantumness [38]. Nuisance-parameter and semiparametric estimation theories explain why treating an unknown loss rate as perfectly calibrated can overstate Kerr precision [39, 40]. We therefore report the Schur complement of the loss block of the QFIM, alongside a concrete classical Fisher matrix. The scalar nuisance benchmark and simultaneous saturation of the entire covariance matrix are kept distinct.

The physical ingredients can be related to established cavity and circuit-QED methods. The Jaynes–Cummings and Tavis–Cummings models organize photon exchange and collective bright states [41, 42]. Circuit-QED theory, transmon design, and strong-coupling experiments motivate controllable multilevel emitters in a resonator [43–46]. Photon-number resolution and observation of the Jaynes–Cummings ladder supply relevant examples of coherent light–matter control [47, 48]. Optical atom–cavity networks provide a different experimental setting [49]. These works support the ingredients rather than establishing a realized implementation of the complete sensing protocol. In particular, both ladder transitions must be compatible with the selected mode or with an appropriately engineered dressed-state description.

Fock-state generation and arbitrary resonator-state synthesis make a fixed two-photon preparation a meaningful theoretical input [50, 51]. Higher-dimensional quantum logic and qudit versions of the Jaynes–Cummings interaction demonstrate the importance of controlling extra levels [52, 53]. Three-level tomography shows how the required atomic population measurements can be organized [54]. Mutually unbiased bases, conventional state reconstruction, and likelihood-based estimation offer explicit alternatives to an unspecified optimal detector [55–59]. Continuous-measurement estimation addresses another readout class [60]; here we restrict the protocol to one atomic measurement after each finite interaction. No continuously monitored photon record is retained.

The resulting model supports several concrete questions. What minimum excitation resource allows the atoms to respond to a normally ordered Kerr term? When does a resonance symmetry make Kerr sign inaccessible? How much information is lost when the cavity is traced out, and how much further is lost through population readout? Does a third level outperform a two-level benchmark after both devices receive the same coupling budget and independent detuning optimization? We

answer these questions with an excitation-sector construction, unconditional Lindblad propagation, exact parameter sensitivities, and finite-sample likelihood tests. The mechanical extension then asks how a calibrated radiation-pressure coupling, finite thermal occupation, and uncertain coupling calibration modify those reference conclusions. The main contribution is a model-specific account of atomic accessibility and its limitations in a hybrid Kerr optomechanical system. We make no claim of a universal multilevel advantage or a first demonstration of atomic Kerr sensing.

2 Hamiltonian model and unconditional dynamics

2.1 Two cascade atoms in a Kerr optomechanical cavity

Each atom $j = A, B$ has states $|0\rangle_j$, $|1\rangle_j$, and $|2\rangle_j$, with energies 0, $\hbar\omega_{10}$, and $\hbar(2\omega_{10} + \alpha)$. The adjacent upper transition has frequency $\omega_{21} = \omega_{10} + \alpha$. We define $\sigma_{pq}^{(j)} = |p\rangle_j\langle q|$, the photon number $n = a^\dagger a$, and the excitation operator

$$N = n + \sum_{j=A,B} (\sigma_{11}^{(j)} + 2\sigma_{22}^{(j)}). \tag{1}$$

For identical real transition couplings, the rotating-wave Hamiltonian in the laboratory frame is

$$\begin{aligned} H/\hbar = {} & \omega_c n + \chi n(n-1) + \omega_m b^\dagger b - g_{\rm om} n(b + b^\dagger) + \sum_{j=A,B} [\omega_{10}\sigma_{11}^{(j)} + (2\omega_{10} + \alpha)\sigma_{22}^{(j)}] \\ & + \sum_{j=A,B} [g_{01} a\sigma_{10}^{(j)} + g_{12} a\sigma_{21}^{(j)} + \text{H.c.}]. \end{aligned} \tag{2}$$

The exchange terms are multilevel extensions of the Jaynes–Cummings and collective-cavity interactions [41, 42]. The self-Kerr description follows nonlinear quantum optical models [16]; controlled multilevel couplings are motivated by circuit-QED methods [45]. The dissipative generator below follows the completely positive Lindblad construction [61]. The mechanical annihilation operator b obeys $[b, b^\dagger] = 1$. The displacement coupling $g_{\rm om}$ is the single-photon radiation-pressure strength, with the sign fixed by the displacement coordinate [26]. The reference g_0 below denotes atomic exchange, not optomechanical coupling. The atoms are held at fixed coupling positions; modulation of their couplings by mechanical displacement is neglected.

Taking $g_0 = g_{01}$ as a common frequency unit, we introduce

$$\tau = g_0 t, \quad x = \chi/g_0, \quad k = \kappa/g_0, \quad \delta = (\omega_{10} - \omega_c)/g_0, \quad \eta = \alpha/g_0, \quad r = g_{12}/g_0. \tag{3}$$

In the frame rotating with $\omega_c N$, the dimensionless Hamiltonian is

$$\begin{aligned} \mathcal{H} = {} & xn(n-1) + \Omega b^\dagger b - \zeta n(b + b^\dagger) \\ & + \sum_j [\delta\sigma_{11}^{(j)} + (2\delta + \eta)\sigma_{22}^{(j)}] \\ & + \sum_j (a\sigma_{10}^{(j)} + ra\sigma_{21}^{(j)} + \text{H.c.}). \end{aligned} \tag{4}$$

The mechanical variables are

$$\Omega = \omega_m/g_0, \qquad \zeta = g_{\rm om}/g_0, \qquad \gamma_m = \Gamma_m/g_0. \tag{5}$$

The identity $[\mathcal{H}, N] = 0$ still holds because radiation pressure preserves photon number. It determines the exact optical and atomic sector, while imposing no phonon-number bound. The known controls

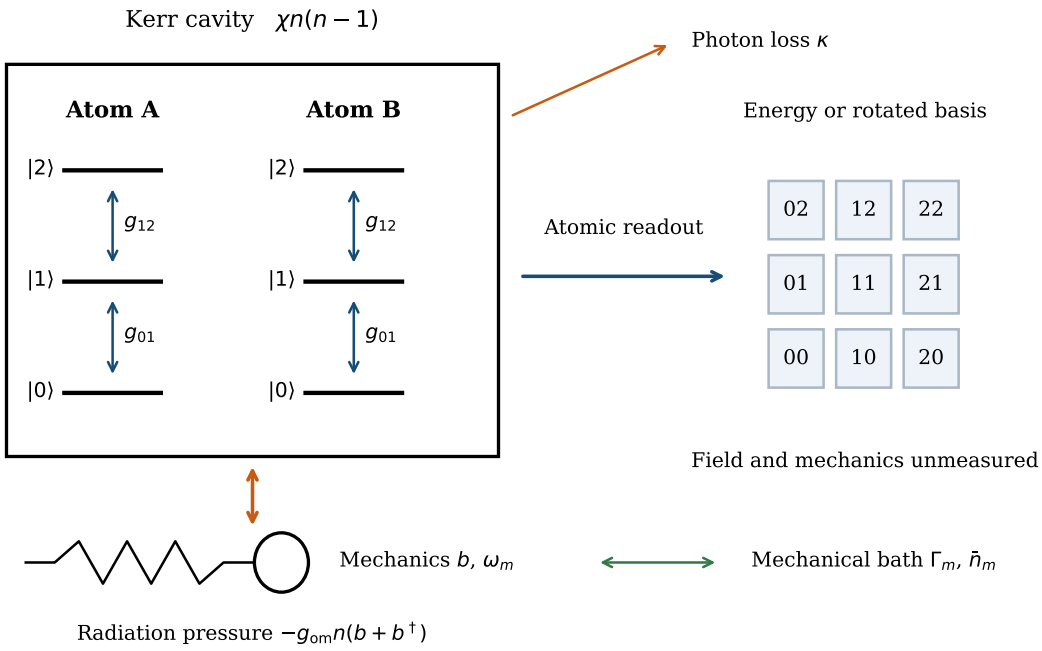


Figure 1: Two identical cascade atoms exchange excitations with a common Kerr cavity coupled by radiation pressure to a mechanical oscillator. The cavity field, mechanical motion, and bath emission records are unmeasured. The final detector records atomic outcomes, either in the energy basis or after calibrated local rotations. The full nine-outcome detector space is shown; some energy-basis outcomes have zero probability in the two-excitation preparation.

are δ, η, and r; the unknown parameters are (x, k). Unless stated otherwise, Ω, ζ, γ_m, the mechanical thermal occupation $\bar{n}_m$, the frequency reference g_0, and atomic relaxation rates are independently calibrated. This assumption is required for the two-parameter interpretation; calibration errors would introduce additional nuisance parameters.

2.2 Optical loss and thermal mechanical dissipation

The optical and atomic reservoirs are at zero temperature, whereas the mechanical reservoir has mean occupation $\bar{n}_m$. We use

$$\begin{aligned}\frac{d\rho}{d\tau} = \mathcal{L}\rho = & -i[\mathcal{H},\rho] + k\mathcal{D}[a]\rho + \gamma\sum_j \mathcal{D}[\sigma_{01}^{(j)}]\rho \\ & + 2\gamma\sum_j \mathcal{D}[\sigma_{12}^{(j)}]\rho + \gamma_m(\bar{n}_m+1)\mathcal{D}[b]\rho + \gamma_m\bar{n}_m\mathcal{D}[b^\dagger]\rho.\end{aligned} \tag{6}$$

where $\mathcal{D}[c]\rho = c\rho c^\dagger - \{c^\dagger c, \rho\}/2$. Thus κ denotes the photon-number decay rate, rather than an amplitude-decay rate with an additional factor of two. The known lower and upper atomic population-decay rates are γg_0 and $2\gamma g_0$, respectively. The latter choice is an explicit oscillator-like relaxation model, not a universal atomic branching rule.

Completely positive dynamical semigroups and the Markov approximation provide the general framework [61–63]. Standard input–output theory describes leakage into a broad-band output bath [64]. Quantum-jump approaches offer an equivalent trajectory interpretation when the complete ensemble is retained [65–67]. Equation (6) assumes approximately flat bath spectra over the relevant dressed transition frequencies and ignores pure atomic dephasing, thermal optical

excitation, collective free-space decay, and frequency dependence of κ. Mechanical heating is included explicitly. The local mechanical dissipator is a phenomenological bath model. Complete positivity alone does not establish a microscopic thermal description: dressed-state relaxation and photon-number-dependent dephasing can matter in nonlinear optomechanics [68], and local bath equations can fail thermodynamic consistency in some parameter regimes even at weak coupling [69]. The numerical results below are therefore conditional on Eq. (6); weak reservoir coupling alone is not offered as proof that this generator describes a particular device. We do not infer heat currents, efficiencies, or thermodynamic consistency from the QFI calculation. No strong-drive linearization is made, and the full operator $n(b + b^\dagger)$ is retained. No normalized no-jump state is substituted for the unconditional state, and there is no postselection on unobserved emissions.

The rotating-wave approximation requires g_{01}, g_{12}, $|\chi|$, $|\alpha|$, and the relevant detunings to remain small compared with optical or microwave carrier frequencies. A single mode coupling both adjacent transitions presupposes an approximately harmonic or engineered ladder. The positive η used in the main numerical example is a stated model choice. An undressed transmon generally has negative anharmonicity, so translating that example to a particular device requires an appropriate level-engineering procedure or a new calculation at the measured spectrum. We do not assign dimensional experimental rates to the chosen dimensionless point.

2.3 Preparation and exact excitation sector

The preparation is a parameter-independent product state,

$$\rho(0) = |00, 2\rangle\langle 00, 2| \otimes \rho_m^{\mathrm{th}}, \qquad \rho_m^{\mathrm{th}} = \sum_{m=0}^{\infty} \frac{\bar{n}_m^m}{(1 + \bar{n}_m)^{m+1}} |m\rangle\langle m|. \tag{7}$$

It contains no initial atom–atom entanglement. Hamiltonian exchange and mechanical jumps preserve N, while optical and atomic jumps lower it. The atom–field register therefore remains in the span of $|a, b, n\rangle$ with $a + b + n \leq 2$, of dimension $1 + 3 + 6 = 10$. The full hybrid basis is $|a, b, n\rangle \otimes |m\rangle$ with unbounded m. Numerics retain $m = 0, \ldots, M - 1$, giving dimension $10M$, and normalize the truncated initial thermal probabilities. This is an exact optical restriction with a separately converged mechanical approximation. The construction includes both symmetric and antisymmetric atomic states, so it remains valid when independent atomic jumps destroy a pure bright-state description.

The measured state and its parameter derivatives are

$$\rho_{\mathrm{at}} = \mathrm{Tr}_{F,m}\, \rho, \qquad \partial_\mu \rho_{\mathrm{at}} = \mathrm{Tr}_{F,m}(\partial_\mu \rho), \quad \mu \in \{x, k\}. \tag{8}$$

The subscript at denotes the complete two-atom register. All atomic information calculations use the full 9×9 reduced matrix. The joint state includes the atoms, cavity, and mechanics after all output reservoirs have been discarded. The intermediate state $\rho_{\mathrm{at},F} = \mathrm{Tr}_m\, \rho$ is also retained for an information-access comparison. Neither state is a purification including emitted bath quanta. For $\zeta = 0$, mechanics factors out and the joint QFIM reduces to the original atom–cavity matrix.

3 Parameter information and specified measurements

3.1 Exact sensitivity propagation

Let $S_\mu = \partial_\mu \rho$. Parameter differentiation of Eq. (6) gives

$$\begin{aligned} \dot{S}_x &= \mathcal{L} S_x - i[n(n-1), \rho], \\ \dot{S}_k &= \mathcal{L} S_k + \mathcal{D}[a]\rho, \qquad S_x(0) = S_k(0) = 0. \end{aligned} \tag{9}$$

Dots denote τ derivatives. These linear inhomogeneous equations are propagated together with the state through one block generator. The method avoids choosing a finite-difference step during the main calculation; finite differences are reserved for an independent validation. Similar derivative propagation has been used in Kerr multiparameter estimation [22]. The Hamiltonian and rates are constant during each interrogation, so a sparse matrix exponential evaluates the augmented system without a time-stepping approximation.

3.2 Quantum Fisher matrix and unknown loss

For any measured density operator ϱ, the symmetric logarithmic derivatives satisfy

$$2\partial_\mu \varrho = \varrho L_\mu + L_\mu \varrho, \qquad F_{\mu\nu} = \frac{1}{2} \operatorname{Tr}[\varrho (L_\mu L_\nu + L_\nu L_\mu)]. \tag{10}$$

Writing $\varrho = \sum_l \lambda_l |l\rangle\langle l|$, we compute

$$F_{\mu\nu} = 2 \sum_{\lambda_l + \lambda_m > 0} \frac{\operatorname{Re}\left[\langle l|\partial_\mu \varrho|m\rangle\langle m|\partial_\nu \varrho|l\rangle\right]}{\lambda_l + \lambda_m}. \tag{11}$$

For the preparation in Eq. (7), neither unknown parameter is encoded at the initial instant. Consequently,

$$S_x(0) = S_k(0) = 0, \qquad F^{\text{atoms}}(0) = F^{\text{joint}}(0) = \begin{pmatrix} 0 & 0 \\ 0 & 0 \end{pmatrix}.$$

This zero is an exact initial condition, not a plotting convention. The parameters being estimated are the interaction strength and loss rate, rather than an initially encoded phase. The Kerr operator initially acts as $n(n-1)|00, 2, m\rangle = 2|00, 2, m\rangle$, so its immediate phase is global. Excitation exchange must first create amplitudes with different photon occupations before relative Kerr phases can change atomic outcomes. The atomic loss response likewise develops only after information is transferred from the cavity.

The calculated atomic Kerr entry rises from $F_{xx}(0) = 0$ to 6.27037×10^{-10} at $\tau = 0.05$, 2.91731×10^{-4} at $\tau = 0.4$, and 2.73121 at $\tau = 3.2$ for the zero-mechanical-coupling operating point specified in Section 5. The same exactly zero initial QFI holds for the hybrid preparation, since its thermal state is also independent of (x, k). The small early-time values can appear flat on a linear vertical scale. At zero time the information matrix is singular; information ratios and information per unit time are therefore left undefined there, and no finite initial precision bound is inferred by dividing by zero.

The same expression is applied to the joint state and the atomic state. For locally unbiased estimators at a regular identifiable point, the matrix SLD bound is $V \succeq F^{-1}/N_{\text{rep}}$ for N_{rep} independent repetitions. An unknown loss rate modifies the scalar Kerr bound through

$$F_{x|k} = F_{xx} - \frac{F_{xk}^2}{F_{kk}}, \qquad \operatorname{Var}(\hat{x}) \geq \frac{1}{N_{\text{rep}} F_{x|k}}. \tag{12}$$

The inequality is an SLD lower benchmark. We do not replace a singular information matrix with a pseudoinverse and interpret it as successful two-parameter estimation. A zero Schur complement denotes absence of regular Kerr identifiability with unknown loss at that interrogation point. Nuisance-parameter and semiparametric theories justify this separation [39, 40].

For fixed physical interrogation time, $F_{\chi\chi} = F_{xx}/g_0^2$, $F_{\kappa\kappa} = F_{kk}/g_0^2$, and $F_{\chi\kappa} = F_{xk}/g_0^2$. All plotted matrices refer to dimensionless (x, k). When preparation and readout overhead are neglected, the information rate is

$$\mathcal{R}_x = F_{x|k}/\tau. \tag{13}$$

It corresponds to repeated shots within a fixed interrogation-time budget. A real experiment with overhead τ_0 should optimize $F_{x|k}/(\tau + \tau_0)$ instead. Per-shot information and information per total laboratory time therefore need not have the same optimum.

3.3 Accessibility and compatibility

Partial trace is independent of (x, k) and cannot increase the QFIM. Thus

$$F^{\text{atoms}} \preceq F^{\text{at},F} \preceq F^{\text{joint}}, \qquad \mathcal{A}_x = \frac{F^{\text{atoms}}_{x|k}}{F^{\text{joint}}_{x|k}} \leq 1 \tag{14}$$

at regular points. The matrix ordering implies the scalar Schur-complement ordering because inversion reverses the positive-definite matrix order. This fraction assesses access to the retained cavity and mechanical information. The intermediate matrix separates the further loss caused by tracing mechanics. It does not quantify information already lost to external reservoirs.

We calculate the mean SLD commutator and its normalized magnitude,

$$D_{xk} = \frac{1}{2i}\,\mathrm{Tr}[\varrho[L_x, L_k]], \qquad \mathcal{Q} = \frac{|D_{xk}|}{\sqrt{\det F}}. \tag{15}$$

For regular two-parameter models $0 \leq \mathcal{Q} \leq 1$. A nonzero value rules out simultaneous saturation of the full SLD matrix bound; it does not by itself forbid attaining the scalar bound for one parameter of interest using suitable adaptive strategies [33, 36, 38, 39]. We do not evaluate the complete Holevo optimization, and consequently do not identify F^{-1} with the attainable joint quantum covariance when $D_{xk} \neq 0$.

3.4 Atomic population readout and local basis mixtures

The simplest detector resolves both atomic energy levels. Its probabilities and classical Fisher matrix are

$$p_{ab} = \langle ab|\rho_{\text{at}}|ab\rangle, \qquad C^{(Z)}_{\mu\nu} = \sum_{p_{ab}>0} \frac{(\partial_\mu p_{ab})(\partial_\nu p_{ab})}{p_{ab}}. \tag{16}$$

Both measured outcomes are retained, while no field outcome is used. The classical effective information $C_{x|k}$ is the Schur complement of C_{kk}. It determines the usual asymptotic covariance benchmark for an identifiable classical model and is directly testable by simulated counts.

We also consider calibrated local rotations drawn from the four mutually unbiased qutrit bases: the energy basis and the three bases

$$|u^{(a)}_b\rangle = \frac{1}{\sqrt{3}} \sum_{m=0}^{2} \exp\!\left[\frac{2\pi i}{3}(am^2 + bm)\right] |m\rangle, \quad a, b \in \{0, 1, 2\}. \tag{17}$$

This construction gives sixteen product settings for the two atoms [55, 56]. If the setting label

is retained and fractions w_s of shots are assigned to setting s, the per-shot classical matrix is $C(w) = \sum_s w_s C^{(s)}$. We maximize its Schur complement subject to $w_s \geq 0$ and $\sum_s w_s = 1$. A uniform mixture is included as a nonoptimized comparison. These are specific local measurement families, not an optimization over all local positive-operator-valued measurements. Choosing weights near a nominal point requires a preliminary calibration stage, whose cost is excluded from the information-rate figures.

4 Exact sensing restrictions and a controlled benchmark

4.1 Minimum excitation support for Kerr sensing

If both atoms start in their ground states and the initial field is supported only on $n = 0, 1$, every accessible state has $N \leq 1$. On that entire sector, $n(n-1) = 0$. Consequently, $\partial_x \mathcal{L} = 0$ there, and Eq. (9) gives

$$S_x(\tau) = 0, \qquad F_{xx}^{\text{joint}} = F_{xx}^{\text{atoms}} = 0. \tag{18}$$

This result includes all loss trajectories and arbitrary mechanical occupations: the radiation-pressure interaction cannot create a second optical or atomic excitation. Mechanical phonons do not replace the required two-photon optical resource. It also covers arbitrary mixtures or superpositions of the zero- and one-photon inputs under the stated ground-state preparation. It does not apply when initially excited atoms can emit two photons, when a drive adds excitations, or when a linear χn shift is included in the signal Hamiltonian. Two photons are the minimal resource for the present preparation.

4.2 A reference resonance symmetry and the role of the third level

The resonance symmetry and the finite bright-state matrices in this subsection refer to $\zeta = 0$. They are not asserted for the full optomechanical generator with nonzero ζ. Without atomic relaxation, coherent evolution in the symmetric $N = 2$ manifold can be represented in the ordered states $|00, 2\rangle$, $|S_{01}, 1\rangle$, $|11, 0\rangle$, and $|S_{02}, 0\rangle$, where $|S_{0l}\rangle = (|0l\rangle + |l0\rangle)/\sqrt{2}$. Its matrix is

$$\mathcal{H}_2 = \begin{pmatrix} 2x & 2 & 0 & 0 \\ 2 & \delta & \sqrt{2} & r \\ 0 & \sqrt{2} & 2\delta & 0 \\ 0 & r & 0 & 2\delta + \eta \end{pmatrix}. \tag{19}$$

When $\eta = 0$, the two atom-only states have equal energies. Only the bright combination

$$|B\rangle = \frac{\sqrt{2}|11\rangle + r|S_{02}\rangle}{\sqrt{2 + r^2}} \tag{20}$$

couples to $|S_{01}, 1\rangle$. The orthogonal combination remains unpopulated under this preparation and cavity loss alone. At $\delta = 0$, the reduced bright-sector Hamiltonian has diagonal entries $(2x, 0, 0)$ and real nearest-neighbor couplings. An antiunitary symmetry maps x to $-x$ while preserving the transition probabilities. The atomic state then has the form

$$\rho_{\text{at}}(x) = p_0(x)|00\rangle\langle 00| + p_1(x)|S_{01}\rangle\langle S_{01}| + p_2(x)|B\rangle\langle B|, \qquad p_l(x) = p_l(-x). \tag{21}$$

The sign of x is therefore globally inaccessible from this atomic statistical family. At regular interrogation points, $\partial_x \rho_{\text{at}}|_{x=0} = 0$ and the SLD QFI vanishes. At rank-changing exceptional points, the limit of a Fisher information can differ from its value exactly at the singular point [70];

our plotted comparison uses a regular finite-loss point. A proof including cavity loss is given in Appendix A.

Known detuning breaks the symmetry by shifting atomic energies relative to the nonlinear cavity sector. Nonzero η further separates $|11\rangle$ from $|S_{02}\rangle$, so their coherent evolution supplies an additional parameter-dependent structure. The third level can therefore change both population transfer and atomic coherences. That mechanism motivates testing its sensing performance, but does not predetermine a positive advantage after resource normalization.

4.3 Equal interaction strength for two-level atoms

For a fair reference within the accessible excitation support, we match the operator norm of the exchange Hamiltonian. With two identical qutrits, its largest norm in $N \leq 2$ is $g_0\sqrt{6+r^2}$. For two identical qubits with coupling g_q, it is $\sqrt{6}g_q$. We set

$$g_q = g_0\sqrt{\frac{6+r^2}{6}}, \qquad r=\sqrt{2} \implies g_q = \sqrt{\frac{4}{3}}g_0. \tag{22}$$

Both models have the same initial two-photon state, carrier frequency, Kerr strength, cavity loss, lower-transition atomic decay, and interrogation-time range. The qubit reference is represented in its exact eight-dimensional $N \leq 2$ space. Its detuning is optimized independently. Matching the norm is a specific resource convention for these few-excitation dynamics, not a universal comparison of experimental fabrication or control costs. The norm identity is derived in Appendix B.

5 Reference results without mechanical coupling

All results in this section and Figures 2–8 set $\zeta = 0$. An independent thermal mechanical state then factors from the atom–field evolution, so the reference calculations remain unchanged. In particular, the qutrit–qubit improvements and the 200-experiment likelihood study below are zero-coupling controls; they are not new optimization or finite-sample claims for nonzero mechanical coupling.

5.1 Operating point and information transfer

Unless stated otherwise, the numerical parameters are

$$(x, k, \delta, \eta, r, \gamma) = (0.35, 0.08, 0.4, 0.6, \sqrt{2}, 0.005). \tag{23}$$

We sample $0 \leq \tau \leq 6$ in steps of 0.05, including the exact zero-information initial point. Figure 2 compares the atomic and joint information. The cavity retains a substantial part of the signal: both diagonal QFIM entries and the Kerr Schur complement are larger for the joint state. Atomic information oscillates as excitation exchange changes which part of the state carries parameter distinguishability. The corresponding accessibility fraction is not constant in time, so choosing a large joint QFI is insufficient for choosing an atomic interrogation time.

At $\tau = 3.2$, the atomic matrix and effective information are

$$F^{\text{atoms}} = \begin{pmatrix} 2.73121 & 1.66218 \\ 1.66218 & 18.49174 \end{pmatrix}, \qquad F^{\text{atoms}}_{x|k} = 2.58180. \tag{24}$$

The joint effective information is 3.50563, giving $\mathcal{A}_x = 0.7365$. The atomic nuisance penalty reduces the known-loss Kerr information by approximately 5.47% at this point. At $\tau = 5.45$, the atomic effective information reaches 5.25352 and its sampled information rate is 0.96395; the joint effective

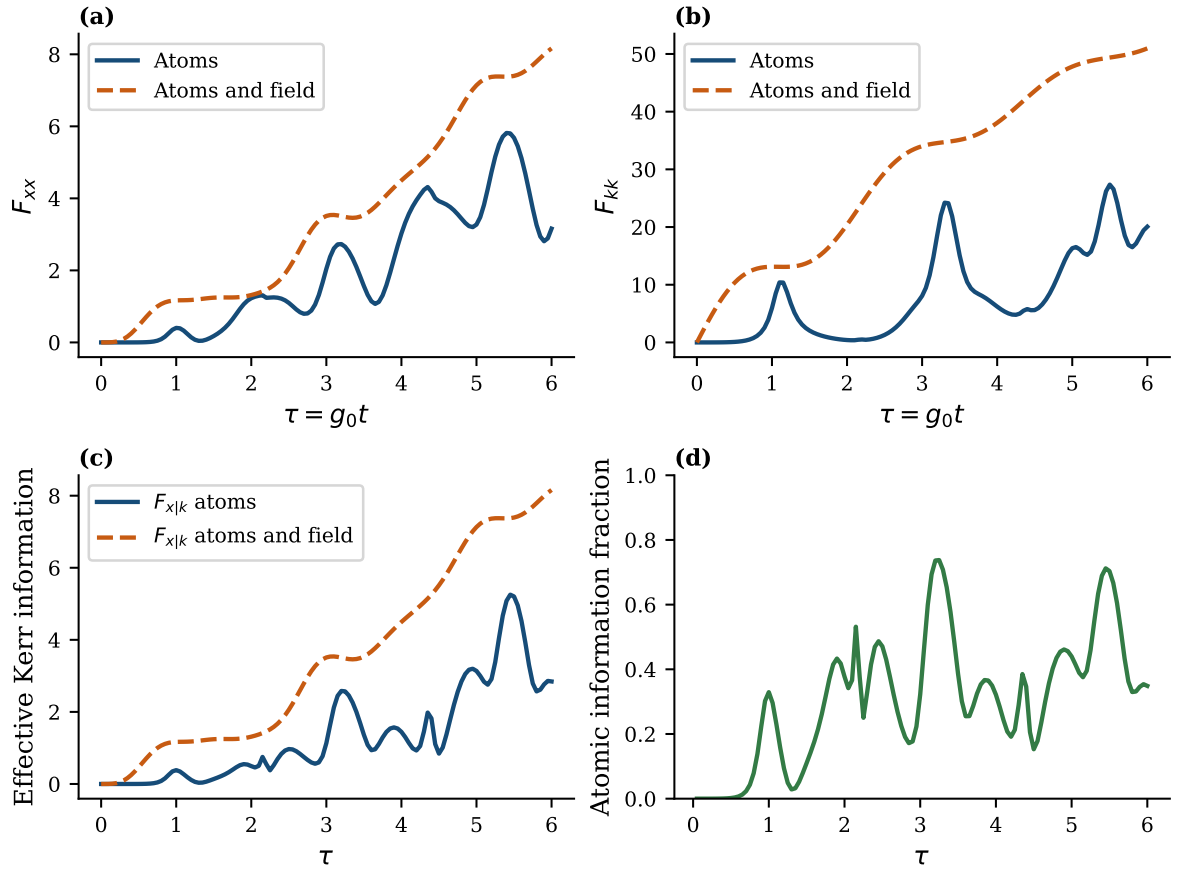


Figure 2: Information transfer at Eq. (23). (a) Kerr diagonal QFI. (b) Loss diagonal QFI. (c) Kerr information with unknown loss. Solid blue curves refer to atomic readout access; dashed orange curves refer to the joint atom–field state. (d) Atomic fraction of the joint effective Kerr information. Both states are unconditional and the external output bath is traced out. Absolute information curves include $\tau = 0$; the information fraction is undefined at that singular point.

information is 7.37688. These values depend on the declared time range and operating point. They are not asymptotic steady-state sensitivities.

5.2 Removing the regular Kerr blind point

Figure 3 fixes $\tau = 1.2$, $k = 0.08$, and $\gamma = 0$, and compares three known atomic spectra. The resonant harmonic ladder has an even atomic response and vanishing regular QFI at $x = 0$, as predicted by Eq. (21). A detuned harmonic ladder with $\delta = 0.4$ has $F_{xx} = 0.33812$ at $x = 0$. Retaining the same detuning and setting $\eta = 0.6$ increases that value to 0.48369. The energy-population Fisher information is nearly identical to the atomic diagonal QFI at this particular time, but this closeness does not imply equality of the complete multiparameter models at all times.

The displaced minima in the detuned curves illustrate how a known control can move an unfavorable operating region. Their position follows the competition between the nonlinear energy $2x$ of $|00, 2\rangle$ and the atomic energies in Eq. (19). The curve with zero detuning cannot distinguish positive and negative Kerr strengths through atomic outcomes, even though it can distinguish their magnitudes away from zero. Practical sign estimation therefore requires a symmetry-breaking preparation or control, and the final inference must be restricted to an identifiable parameter neighborhood.

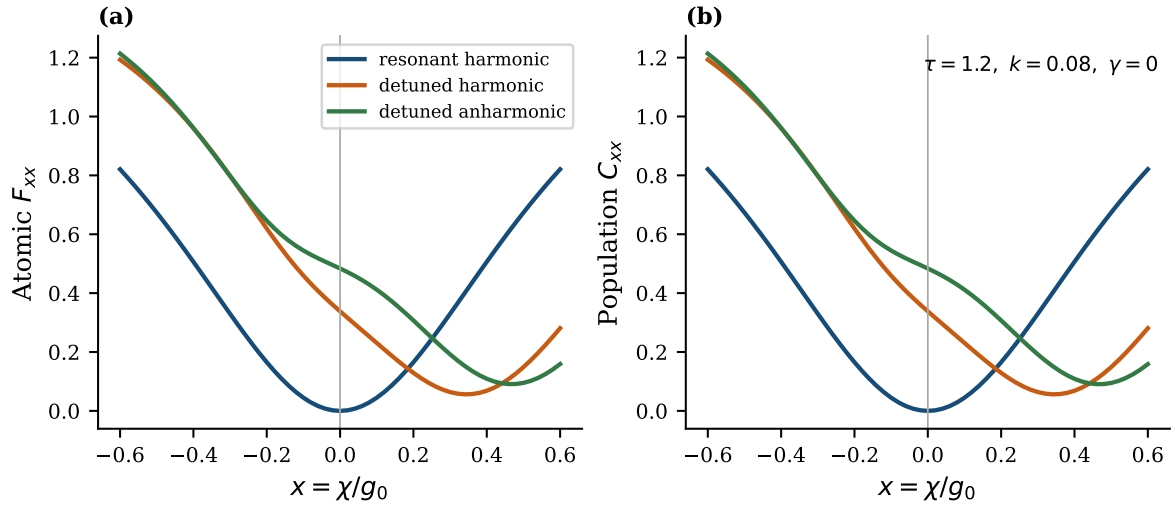


Figure 3: A regular atomic Kerr blind point and its removal. Blue: $(\delta, \eta) = (0, 0)$; orange: $(0.4, 0)$; green: $(0.4, 0.6)$. The common parameters are $\tau = 1.2$, $k = 0.08$, $r = \sqrt{2}$, and $\gamma = 0$. (a) Atomic QFI F_{xx}. (b) Energy-population Fisher information C_{xx}. Kerr strength is the differentiated parameter in each curve, rather than a preparation phase.

5.3 Detuning maps and finite-time operating regions

Figure 4 samples $0 \leq x \leq 0.8$ at 17 points and $-1.2 \leq \delta \leq 1.2$ at 25 points. At each point we maximize $F_{x|k}/\tau$ over 60 interrogation times in $0.1 \leq \tau \leq 4$, keeping the remaining parameters at Eq. (23). The colored regions reveal that the preferred detuning changes with the true Kerr strength and that high sensitivity may require a longer interrogation than other parts of the map. Abrupt changes in the selected time can reflect switching between oscillatory local maxima and the finite time grid.

This map is a sensitivity chart, not an experimental optimization of an unknown x. A detector designer can choose δ and τ after a coarse calibration, or choose settings that perform acceptably across a prior interval. The largest plotted rate, 1.93794, occurs at the boundary $(x, \delta) = (0.8, -1.2)$; it must not be described as a global optimum. The independent two-level comparison below uses a broader detuning interval and a longer time range.

5.4 Feasible measurements and multiparameter incompatibility

Figure 5 distinguishes atomic access from detector performance. At $\tau = 3.2$, energy-population readout yields $C^{(Z)}_{x|k} = 2.23074$, approximately 86.4% of the atomic SLD benchmark. Optimizing the sixteen product-basis weights selects the energy setting alone at this operating point. Across the displayed baseline sequence, the optimized product-basis family gives no material improvement over energy-population readout. Adding settings indiscriminately can reduce information per shot. The uniform mixture is substantially less efficient over much of the displayed interval because it spends repetitions on settings that do not resolve the relevant population changes as effectively.

The mean commutator at $\tau = 3.2$ is $D_{xk} = -0.34817$. Across the sampled baseline interval, $\mathcal{Q}$ reaches approximately 0.2563. Thus the two parameters are not everywhere compatible at the quantum limit. This property differs from the asymptotically compatible driven-resonator model of Ref. [22] and is consistent with the need to examine measurement incompatibility separately for each Kerr model [23]. No direct numerical equivalence to either precedent is implied: our probe, preparation, and accessible subsystem differ.

The nuisance penalty also varies strongly with interrogation time. A high F_{xx} can coexist with

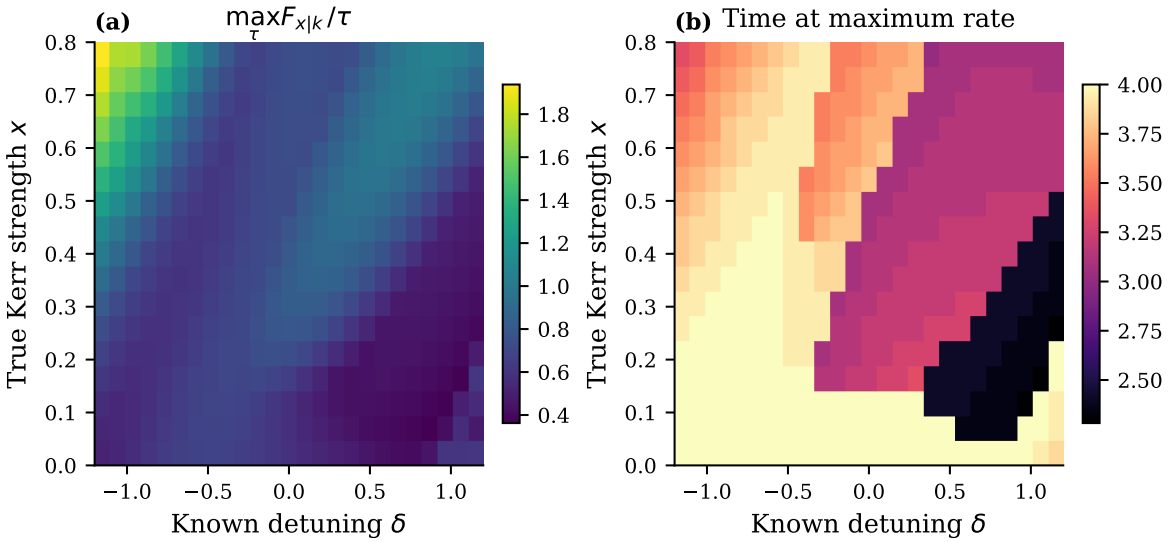


Figure 4: Finite-grid operating maps with $k = 0.08$, $\eta = 0.6$, $r = \sqrt{2}$, and $\gamma = 0.005$. (a) Maximum sampled atomic effective-information rate over $0.1 \le \tau \le 4$. (b) Interrogation time giving that sampled maximum. The vertical coordinate is the true unknown Kerr strength; the horizontal coordinate is a known control. Boundary maxima and time-grid switches do not establish a global control optimum.

Table 1: Best rates found after independent detuning and time refinement at $x = 0.35$, $k = 0.08$, and $\gamma = 0.005$. The qutrit has $\eta = 0.6$ and $r = \sqrt{2}$; the qubit has the norm-matched coupling of Eq. (22).

Probe and criterion	Detuning δ	Time τ	Information rate
Qutrit SLD	−2.03093	4.94991	1.87442
Qubit SLD	−1.59086	4.26313	1.76140
Qutrit populations	−2.12027	4.84321	1.83957
Qubit populations	−1.59221	4.26227	1.76019

a small $F_{x|k}$ when the Kerr and loss response directions are nearly parallel. For practical sensing, the classical Schur complement directly quantifies this ambiguity in the measured outcomes. The SLD curvature, the cavity-access fraction, and the classical measurement ratio diagnose different limitations and should not be combined into a single unspecified sensitivity enhancement.

5.5 The third level after fair control optimization

Figure 6 shows why a shared control point can exaggerate the apparent multilevel benefit. At $\delta = 0.4$, the sampled qutrit and qubit SLD rates are 0.96395 and 0.17474, respectively, which suggests an enhancement factor of approximately 5.52. Their exchange norms are both $2\sqrt{2}g_0$, so this difference does not arise from leaving the qubit coupling at a smaller norm. It does, however, arise partly from an unfavorable detuning for the qubit reference.

We therefore scan both models independently over $-3 \le \delta \le 3$ and $0.1 \le \tau \le 6$. The detuning step is 0.1 and the time step is 0.05. Local continuous refinement from the best grid point gives the best values found in Table 1. The qutrit SLD rate is 1.87442 at $(\delta, \tau) = (-2.03093, 4.94991)$, while the qubit rate is 1.76140 at $(-1.59086, 4.26313)$. The resulting model-specific increase is approximately 6.42%. For population readout, the independently refined rates are 1.83957 and 1.76019, an increase of approximately 4.51%.

The upper-level population in Fig. 6(d) confirms participation of the additional transition during the baseline evolution. Nevertheless, its instantaneous population is not a quantitative witness of sensing advantage: information depends on parameter derivatives, earlier dynamics, and

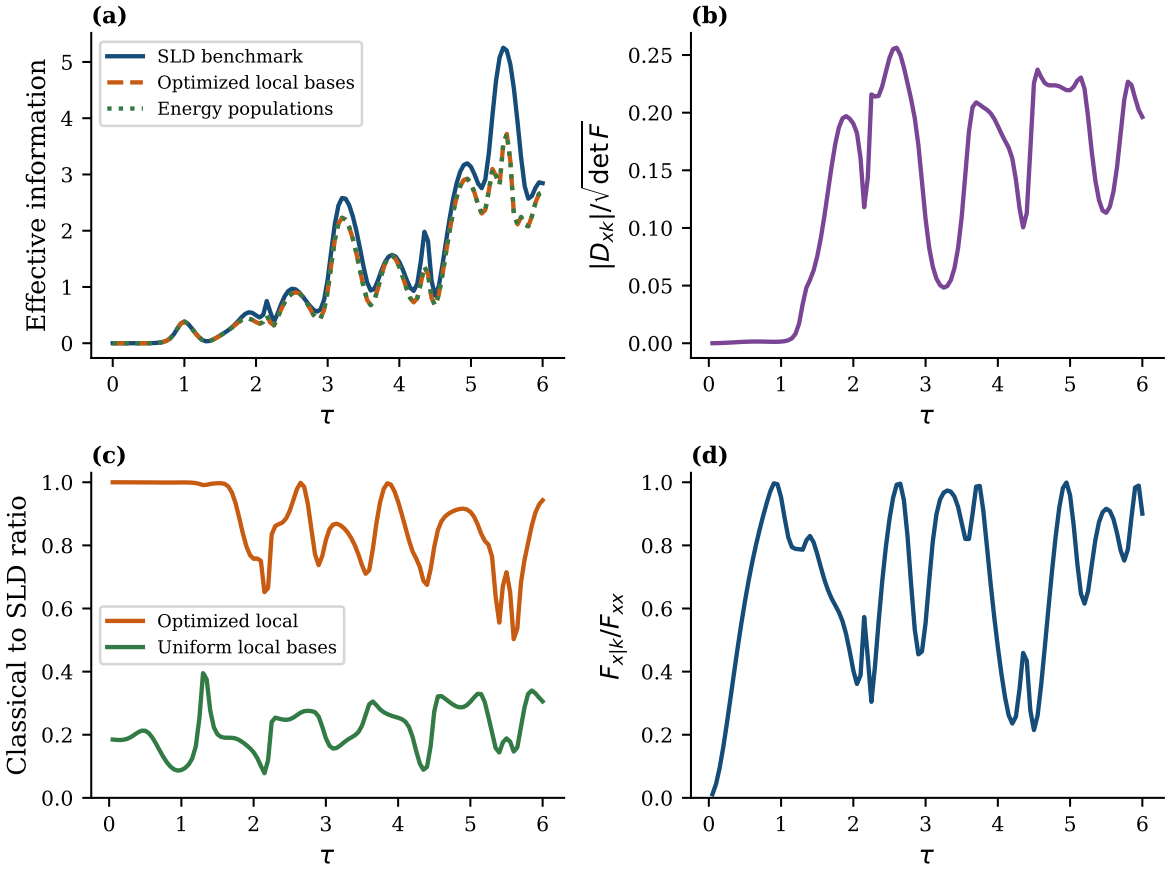


Figure 5: Specified atomic measurements and compatibility at Eq. (23). (a) Atomic SLD Schur complement, optimized local product-basis information, and energy-population information. (b) Normalized mean SLD commutator. (c) Ratios of optimized and uniformly mixed local-basis information to the atomic SLD benchmark. (d) Reduction of Kerr information when cavity loss is unknown. The optimized family contains sixteen settings and does not include arbitrary collective atomic measurements.

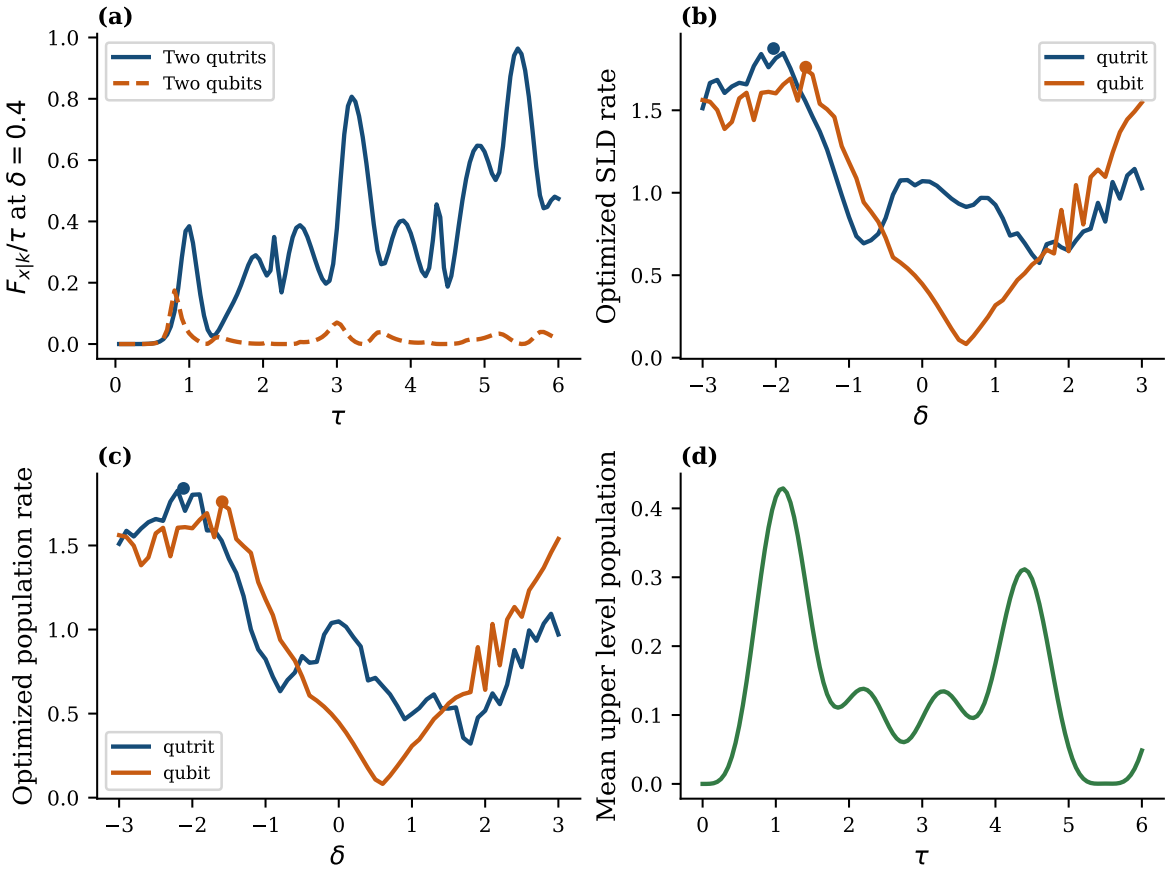


Figure 6: Controlled comparison with two two-level atoms. (a) Effective-information rates at shared detuning $\delta = 0.4$. (b) SLD rates optimized over time for each detuning. (c) Corresponding population-readout rates. Dots denote continuous refinements from the best grid points. (d) Mean total occupation of the two upper atomic levels at the baseline point. Coupling norms, initial photon number, loss, and lower atomic decay are matched; each reference receives its own detuning optimization.

correlations with loss. The independently optimized result supports a modest benefit at the stated spectrum, not a general superiority of qutrit probes. Different anharmonicities, preparation costs, coupling conventions, or readout overhead can alter the ordering. The finite control search and local refinement do not constitute a proof of a global optimum over all preparations and controls.

5.6 Loss and relaxation robustness

Figure 7 varies $0.02 \leq k \leq 0.4$ and compares $\gamma = 0$, 0.005, and 0.02 at fixed $x = 0.35$, $\delta = 0.4$, $\eta = 0.6$, and $r = \sqrt{2}$. Each rate is maximized over the stated $0.1 \leq \tau \leq 4$ window. With $\gamma = 0.005$, the best sampled rate falls from 1.17864 at $k = 0.02$ to 0.23900 at $k = 0.4$. At $k = 0.02$, increasing γ from zero to 0.02 lowers the rate from 1.22402 to 1.04459. The deterioration is therefore quantified rather than replaced by a statement that the third level protects the sensor.

At fixed $\tau = 3.2$, the fraction retained in the atoms and the fraction accessible through populations respond differently to k. A larger measurement ratio can accompany a smaller absolute information, because noise can remove the atomic coherence that was responsible for the difference between population and quantum sensitivity. Ratios should consequently be read together with the absolute rate. The state is not continuously pumped, and the calculations concern transient interrogation. With positive atomic relaxation, the eventual vacuum and atomic ground state carry no regular sensitivity to either parameter; a stationary protection claim would require a different protocol.

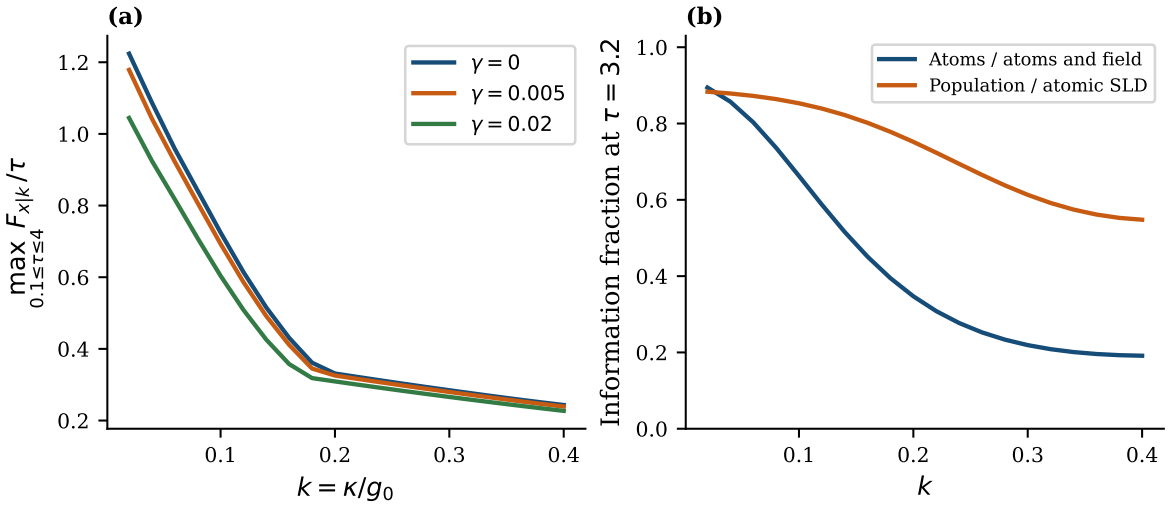


Figure 7: Transient robustness at fixed $x = 0.35$, $\delta = 0.4$, $\eta = 0.6$, and $r = \sqrt{2}$. (a) Effective atomic-information rate maximized over $0.1 \le \tau \le 4$ for three known atomic relaxation strengths. (b) Atomic-to-joint and population-to-atomic information fractions at $\tau = 3.2$, $\gamma = 0.005$. The two fractions quantify different restrictions, and neither alone establishes a gain in absolute precision.

5.7 Simulated joint inference from atomic outcomes

To check whether the classical model supports estimation of both parameters, we generate 200 independent multinomial experiments with 5000 atomic energy outcomes each at Eq. (23) and $\tau = 3.2$. Every experiment is fitted by maximum likelihood for (x, k) in the local calibration neighborhood $0.15 \le x \le 0.55$, $0.015 \le k \le 0.20$. The same fixed initial guess $(0.30, 0.10)$ is used for every fit. The random seed is 20261013. These are simulated detector records, not experimental observations, and the bounded neighborhood does not establish global identifiability over all Kerr signs and loss values.

The means are $(0.34950, 0.08044)$ for true parameters $(0.35, 0.08)$. The sample covariance and the classical Cramér–Rao reference are

$$V_{\mathrm{MC}} = \begin{pmatrix} 9.8250\times10^{-5} & -5.7953\times10^{-6} \\ -5.7953\times10^{-6} & 1.1926\times10^{-5} \end{pmatrix}, \qquad C_Z^{-1}/5000 = \begin{pmatrix} 8.9656\times10^{-5} & -7.0272\times10^{-6} \\ -7.0272\times10^{-6} & 1.1726\times10^{-5} \end{pmatrix}. \tag{25}$$

The empirical standard deviations are approximately 0.00991 for x and 0.00345 for k. The Kerr variance is about 9.6% above its classical reference and the loss variance about 1.7% above it. With only 200 repetitions of the whole experiment, a variance estimate has a sampling fluctuation of order $\sqrt{2/199} \simeq 10\%$ for an approximately Gaussian estimator. This agreement supports feasibility near the specified point without proving finite-sample efficiency, unbiasedness, or performance under detector errors. All likelihood optimizations return successfully with the documented fallback procedure.

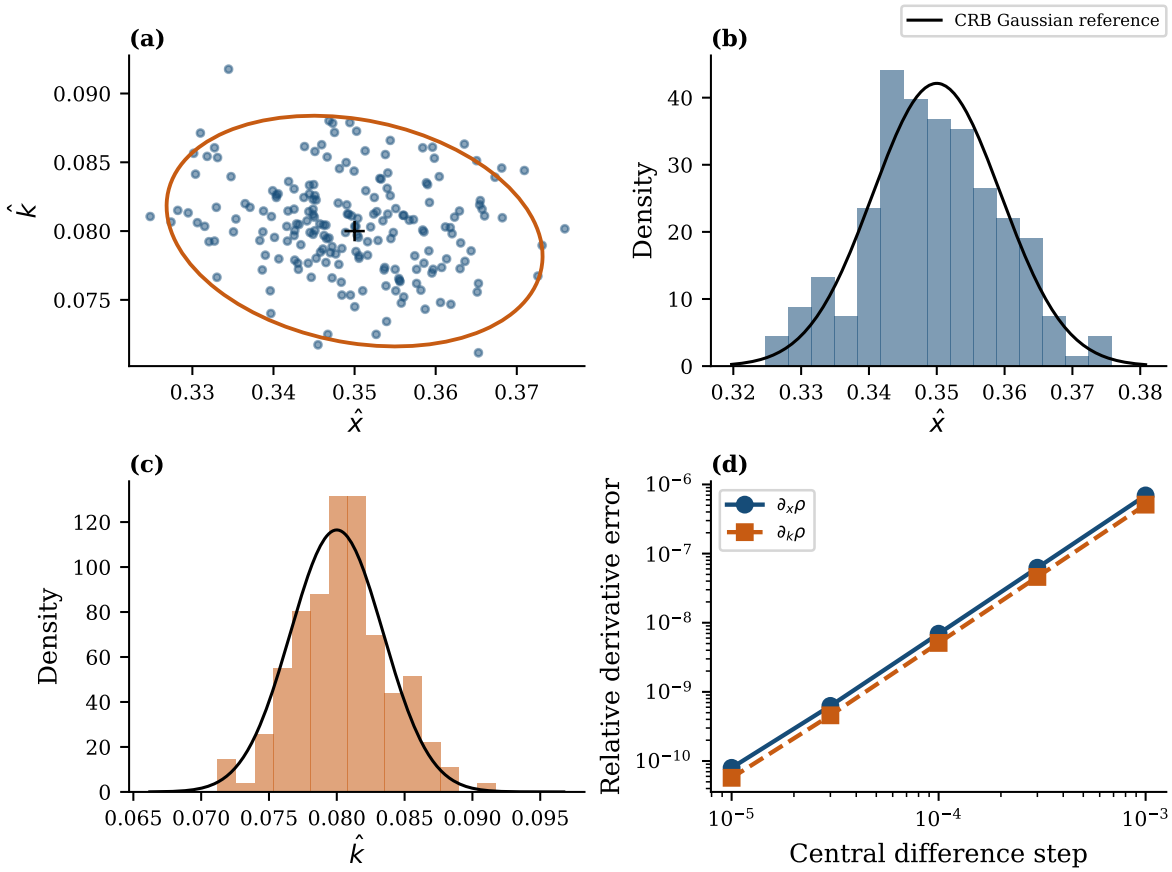


Figure 8: Simulated inference and independent numerical checks. (a) Estimates from 200 experiments, each containing 5000 atomic energy measurements; the cross denotes the true point and the ellipse is the 95% Gaussian covariance reference from the classical Fisher matrix. (b,c) Empirical marginal distributions and Gaussian references. (d) Central finite-difference checks against exactly propagated state derivatives at $\tau = 1.2$. The experiment uses the local bounded neighborhood and seed stated in the text.

6 Optomechanical information transfer and thermal effects

6.1 Mechanical coupling and accessible information

We now retain the full radiation-pressure term. The optical and atomic parameters remain those in Eq. (23), while the default mechanical settings are

$$(\Omega, \zeta, \gamma_m, \bar{n}_m) = (2, 0.35, 0.02, 0.1). \tag{26}$$

The coupling ζ is denoted `G` in the supplied calculation programs. Figure 9 compares $\zeta = 0$, 0.2, 0.35, and 0.5 at fixed known detuning and the same two-photon preparation. Information rates are sampled on $0.05 \le \tau \le 6$ with step 0.05, matching the reference time resolution; no new detuning optimization is performed for these mechanical curves. Their maxima are therefore finite-window sampled values, not globally optimized sensor performances.

At $\tau = 3.2$ and Eq. (26), the atomic matrix and scalar benchmark are

$$F^{\mathrm{atoms}} = \begin{pmatrix} 2.014588 & 1.124143 \\ 1.124143 & 15.984827 \end{pmatrix}, \qquad F^{\mathrm{atoms}}_{x|k} = 1.935532. \tag{27}$$

The effective atom–field and full hybrid values are 2.919430 and 3.206879, respectively. Atomic populations retain $C^{(Z)}_{x|k} = 1.575036$, or approximately 81.4% of the atomic SLD benchmark. Thus only about 60.4% of the retained hybrid Kerr information reaches the atomic register. These quantities follow distinct partial traces and measurements; their differences are not identified with the bath loss alone.

At the same time, increasing ζ from zero to 0.2, 0.35, and 0.5 changes $F^{\mathrm{atoms}}_{x|k}$ from 2.581804 to 2.358379, 1.935532, and 1.399854. The default mechanical coupling therefore lowers the value by approximately 25.0%. The largest sampled rate falls from 0.96395 at $\tau = 5.45$ without coupling to 0.75611 at $\tau = 5.35$ for $\zeta = 0.35$, and 0.55317 at $\tau = 5.2$ for $\zeta = 0.5$. These results establish deterioration at the tested controls and do not exclude gains after different preparation or control optimization. Mean phonon occupation in Figure 9(d) confirms that mechanics is dynamically excited rather than frozen in its initial state.

6.2 Thermal motion and the shifted Kerr approximation

The same known mean occupation $\bar{n}_m$ specifies both the prepared mechanical thermal state and its bath. At $\zeta = 0.35$, increasing it from 0 to 0.1 and 0.5 changes $F^{\mathrm{atoms}}_{x|k}(3.2)$ from 2.089219 to 1.935532 and 1.439812. Figure 10(a) shows the time dependence. This scan varies preparation noise and bath occupation together; it does not distinguish their separate effects or assume that the atoms or optical field are thermal.

A square completion gives the exact operator identity

$$\begin{aligned} xn(n-1) + \Omega b^\dagger b - \zeta n(b + b^\dagger) = \Omega \left(b - \frac{\zeta n}{\Omega}\right)^\dagger \left(b - \frac{\zeta n}{\Omega}\right) \\ + \left(x - \frac{\zeta^2}{\Omega}\right) n(n-1) - \frac{\zeta^2}{\Omega} n. \end{aligned} \tag{28}$$

This identity identifies the induced negative Kerr contribution discussed in optomechanics [27,28]. It does not eliminate mechanics from the full atom–field model: the displacement depends on photon number, exchange changes that number, and mechanical noise remains. A corresponding polaron transformation also dresses the exchange operators. We therefore compare the actual dynamics

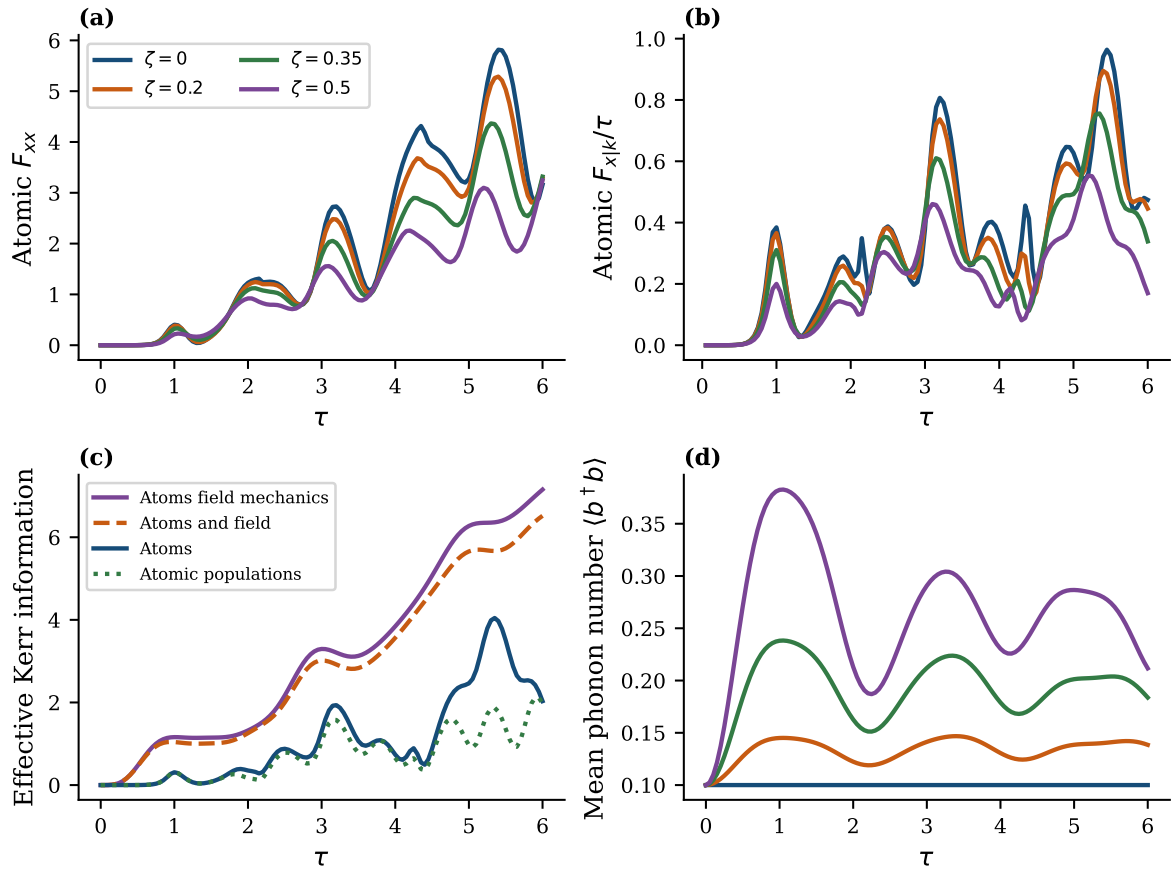


Figure 9: Full optomechanical dynamics at the optical and atomic reference point, $\Omega = 2$, $\gamma_m = 0.02$, $\bar{n}_m = 0.1$, and mechanical dimension $M = 16$. (a) Atomic Kerr QFI for four radiation-pressure couplings. (b) Effective atomic information per unit time, with the undefined zero-time value omitted. (c) Nested full-hybrid, atom–field, atomic, and atomic-population effective information at $\zeta = 0.35$. (d) Mean mechanical occupation for the couplings in (a). Mechanical coupling is calibrated in all panels.

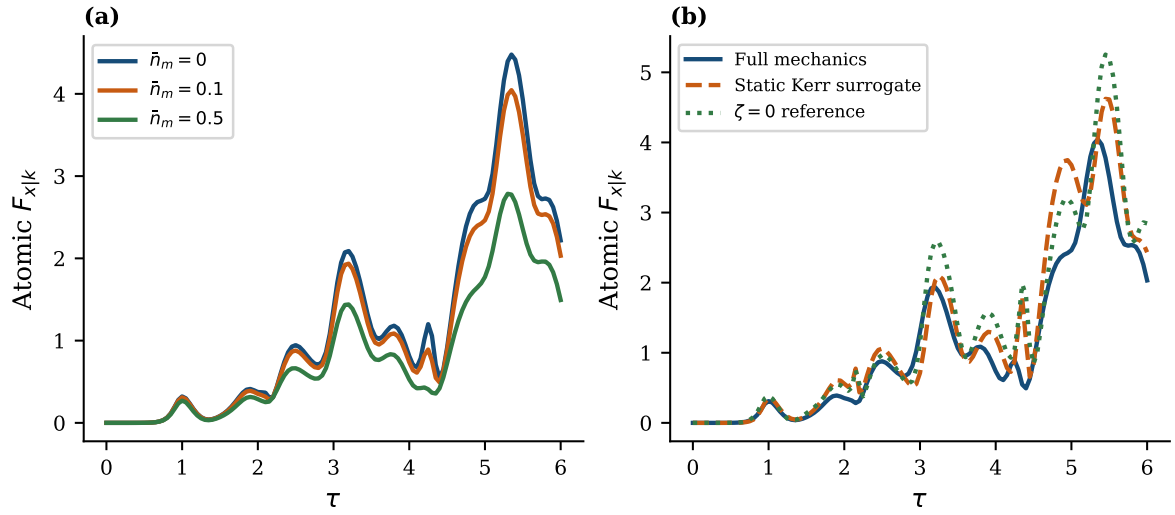


Figure 10: Mechanical thermal occupation and a static approximation. (a) Effective atomic Kerr information for three known mechanical occupations, with $\zeta = 0.35$, $\Omega = 2$, and $\gamma_m = 0.02$. The same occupation sets preparation and bath noise. The $\bar{n}_m = 0.5$ curve uses $M = 24$; the others use $M = 16$. (b) The full hybrid calculation at $\bar{n}_m = 0.1$, the static shifted-Kerr surrogate, and the uncoupled reference. These comparisons keep atomic detuning controls fixed as specified in the text.

with a diagnostic static surrogate that drops the displaced oscillator and uses $x_{\mathrm{eff}} = x - \zeta^2/\Omega$ and $\delta_{\mathrm{eff}} = \delta + \zeta^2/\Omega$ after the linear cavity-frequency shift. The same bare exchange and optical loss are used in that surrogate.

For Eq. (26), the surrogate gives $F_{x|k}(3.2) = 2.026590$, approximately 4.7% above the full-mechanical atomic value. Figure 10(b) shows that a shifted coefficient alone does not reproduce the complete temporal response. This is a test at the stated intermediate frequency and transient preparation, not a denial of effective Kerr descriptions in their appropriate limits. Intrinsic x and mechanically induced nonlinearity must consequently be distinguished when interpreting atomic sensitivity.

6.3 Uncertain mechanical coupling

The preceding two-parameter problem assumes calibrated ζ. The optional three-parameter problem is local to the positive-coupling branch around $\zeta = 0.35$. To quantify this assumption at one regular point, we additionally propagate $S_\zeta = \partial_\zeta \rho$ through

$$\dot{S}_\zeta = \mathcal{L} S_\zeta + i[n(b + b^\dagger), \rho], \qquad S_\zeta(0) = 0. \tag{29}$$

For the three-parameter QFIM with order (x, k, ζ), the scalar benchmark with two nuisance parameters is

$$F_{x|k,\zeta} = F_{xx} - F_{x\nu}(F_{\nu\nu})^{-1} F_{\nu x}, \qquad \nu = (k, \zeta). \tag{30}$$

Only nonsingular nuisance blocks are interpreted this way. At Eq. (26) and $\tau = 3.2$, the atomic benchmark changes from 1.935532 to 1.693180 when ζ is unknown, an additional reduction of approximately 12.5%. The corresponding population value changes from 1.575036 to 1.045425, a reduction of approximately 33.6%. The three atomic QFIM eigenvalues are approximately 0.36652, 1.98582, and 16.21544, so this calculation is at a regular local point. Figure 11(b) compares the two cases. This local nuisance calculation does not constitute a finite-sample three-parameter fit or a simultaneous-attainability claim for the quantum covariance matrix.

The sign restriction follows from an exact mechanical parity symmetry. For $P_m = \exp(i\pi b^\dagger b)$,

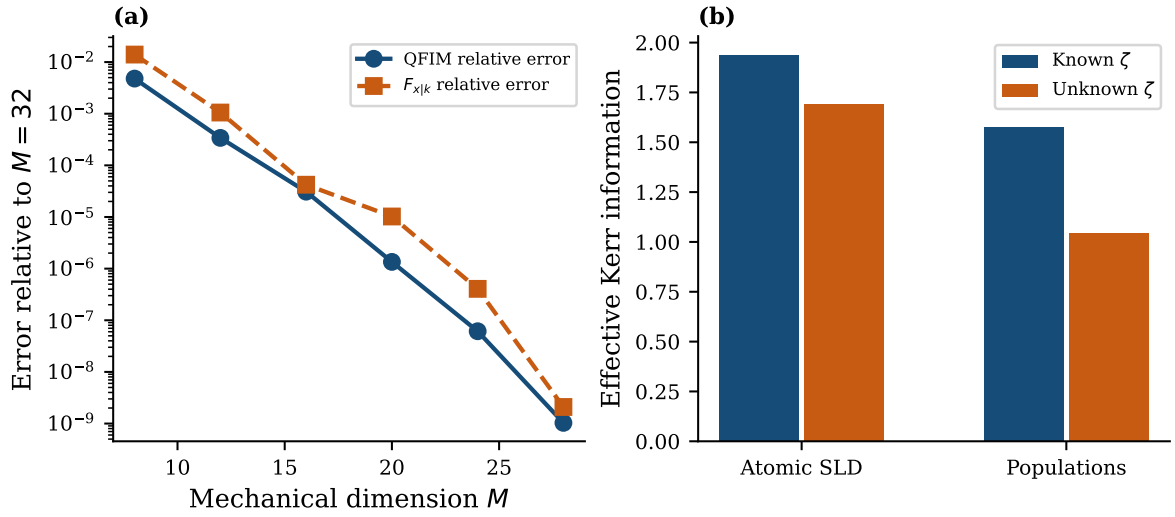


Figure 11: Mechanical convergence and calibration cost. (a) Maximum relative QFIM and effective-information differences from $M = 32$, sampled at $\tau = 1.6$, 3.2, and 6 for the demanding case $\zeta = 0.5$, $\bar{n}_m = 0.5$. (b) Atomic SLD and population effective information at the default mechanical point and $\tau = 3.2$, comparing calibrated and unknown radiation-pressure coupling. Cavity loss is unknown in both cases.

one has $P_m b P_m^\dagger = -b$ and $\mathcal{H}(-\zeta) = P_m \mathcal{H}(\zeta) P_m^\dagger$. The initial thermal state and both mechanical dissipators are parity invariant. Tracing mechanics therefore gives

$$\rho_{\mathrm{at},F}(\zeta) = \rho_{\mathrm{at},F}(-\zeta), \qquad \rho_{\mathrm{at}}(\zeta) = \rho_{\mathrm{at}}(-\zeta).$$

Atomic data cannot identify the global sign of ζ under this preparation. In particular, $\partial_\zeta \rho_{\mathrm{at}} = 0$ at $\zeta = 0$, so the three-parameter first-order model is singular there. This does not remove Kerr sensitivity from the regular two-parameter reference problem in which $\zeta = 0$ is fixed. The stated nuisance penalties concern the nonzero positive branch, not inference across both signs.

6.4 Mechanical basis convergence

Phonon excitation is not restricted by the initial two-photon support. We therefore check mechanical dimensions independently of the exact optical sector. At the default mechanical point, comparisons at $\tau = 1.6$, 3.2, and 6 between $M = 16$ and $M = 24$ give maximum relative QFIM and effective-information differences of 1.53×10^{-11} and 3.79×10^{-11}. The largest top-level population on the default time curve is 3.99×10^{-12}.

A more demanding check uses $\zeta = 0.5$ and $\bar{n}_m = 0.5$. Relative to $M = 32$ at the same three nonzero times, the maximum relative QFIM differences for $M = 12$, 16, 20, 24, and 28 are 3.40×10^{-4}, 3.09×10^{-5}, 1.35×10^{-6}, 6.13×10^{-8}, and 1.03×10^{-9}. Effective-information differences can be larger: the $M = 24$ maximum is 4.06×10^{-7}. Figure 11(a) reports both quantities. Small boundary population alone is not used as the convergence criterion. These checks support the stated digits and sampled cases, rather than guaranteeing one cutoff for arbitrary temperature, coupling, or interrogation time.

7 Numerical verification and reproducibility

The simulation uses NumPy and SciPy sparse matrix exponentiation. The zero-coupling reference equations evolve a 100-component vectorized state and two 100-component sensitivities; with M mechanical levels, each vector has $(10M)^2$ entries. Reduction to the atomic register occurs only

after propagation. The basis is exact for the prepared excitation support, and thus no photon-cutoff extrapolation is needed. Mechanical truncation is independently checked as described above. An independent calculation in the complete $3 \times 3 \times 3$ atom–field space checks that projecting to the ten-state sector has not changed the unconditional dynamics.

Across the baseline time sequence, the largest trace error is 1.49×10^{-14} and the smallest density eigenvalue is -9.38×10^{-15}, consistent with numerical roundoff. At $\tau = 1.2$, the full-space and sector density operators agree to a Frobenius error of 7.65×10^{-16}. A separate dense Liouvillian exponential agrees with the sparse result to 7.94×10^{-16}. The one-photon control produces exactly zero Kerr QFI. The computed differences $F^{\mathrm{joint}} - F^{\mathrm{atoms}}$ and $F^{\mathrm{atoms}} - C^{\mathrm{local}}$ are positive semidefinite throughout the baseline calculation within numerical precision.

The support threshold in Eq. (11) is 10^{-12}. Changing it to 10^{-10} and 10^{-14} leaves the QFIM unchanged at the tested regular times 0.4, 1.2, 3.2, and 5.45. Central differences with steps from 10^{-3} to 10^{-5} validate both sensitivities at three times; the largest relative discrepancy at the coarsest tested step is below 1.8×10^{-6}. Figure 8(d) displays the expected convergence trend. The scripts, arrays, optimization settings, and figure generation commands are included in the accompanying package so these checks and every plotted curve can be reproduced.

For the optomechanical curves, the maximum trace error is 1.89×10^{-15} and the minimum density eigenvalue is -4.18×10^{-16}. The nested QFIM inequalities are satisfied within 3.56×10^{-10}, including support-threshold roundoff for the full hybrid state. At $\tau = 1.2$, central-difference checks with step 10^{-4} give relative full-state sensitivity errors of 6.99×10^{-9} for x and 5.13×10^{-9} for k. Changing the atomic QFI support cutoff among 10^{-10}, 10^{-12}, and 10^{-14} leaves the tested matrix at $\tau = 3.2$ unchanged to displayed precision. Setting $\zeta = 0$ recovers the original atomic density and sensitivities within 1.84×10^{-14} and 6.55×10^{-14}, respectively, at four tested times. The one-photon hybrid control has exactly zero Kerr derivative and QFI. The additional ζ derivative agrees with its step-10^{-4} central difference within 2.46×10^{-8}. An independent MATLAB-compatible sparse-ODE calculation, executed in GNU Octave, agrees with the atomic and atom–field QFIMs within 1.35×10^{-9} and 6.52×10^{-11} at four tested times. The full mechanical results, comparison arrays, and MATLAB programs accompany the manuscript.

An independently constructed $3 \times 3 \times 3 \times 6$ atom–atom–field–mechanical tensor space provides a second hybrid-model check. Direct integration of the matrix master equation and both sensitivities with a DOP853 solver agrees with the 60-state excitation-sector calculation at the same mechanical cutoff: the largest density or sensitivity Frobenius difference at $\tau = 0$, 0.4, 1.2, and 3.2 is 1.34×10^{-9}, and no population or coherence leaks outside the permitted optical sector. The $M = 6$ choice tests the two constructions at a common cutoff; it does not replace the mechanical-convergence tests. Solving the atomic SLD equations as linear systems at the default three-parameter point reproduces the spectral QFIM within 4.62×10^{-14}, with an SLD-equation residual of 3.13×10^{-15}. A separate lossless pure-state Kerr check using a Hamiltonian Fréchet derivative agrees with the density-matrix QFI within 2.00×10^{-15}. These tests verify the stated generator and information calculation, while leaving the microscopic bath assumptions explicit.

8 Physical interpretation and limitations

The two-photon preparation produces a simple information-transfer mechanism. Initially, the Kerr interaction only multiplies the Fock state by an overall phase and carries no observable atomic signal. Exchange then creates superpositions across sectors with different cavity occupations. The nonlinear energy difference between $n = 2$ and $n = 1$ alters excitation-transfer amplitudes, which become measurable atomic populations and coherences. This process is absent with at most one

total excitation. The harmonic resonant reduction shows that even an active nonlinear pathway may preserve a sign ambiguity, while known atomic detuning can remove it.

The distinction between atomic QFI and population information is operational. The former permits arbitrary measurements on the two-atom density operator; the latter uses a specified local energy detector. Joint atomic measurements could access some coherence-dependent information omitted by that detector, but their implementation and cost are not included here. Likewise, the joint atom–field QFI is a reference for an additional cavity measurement, not a precision that the proposed detector achieves. The finite-sample study demonstrates one feasible local inference point under an ideal level-resolving detector. Misclassification, unequal couplings, uncertain detuning, preparation impurity, and an optical thermal background remain additional tasks for a device-level study.

The modest optimized qutrit gain in the $\zeta = 0$ reference is an important restriction on the interpretation. It has not been reoptimized or established for the coupled mechanical cases. The exchange norm is held fixed, but atomic spectra and the number of accessible transition pathways differ. The third level changes coherent routing rather than increasing the initial photon number. Nevertheless, the reported percentage depends on the known anharmonicity and on a limited control family. Preparation time, frequency tuning, and readout gates have no explicit cost in the calculation. We therefore identify a useful example under a defined norm convention, rather than a resource-independent quantum advantage. A stronger claim would require robustness across spectra and control costs, a broader preparation optimization, and a comparison with experimentally realizable qubit strategies.

Our scope is also distinct from a general nonlinear-medium characterization. The loss parameter is treated as a single constant rate, independent of frequency and Kerr strength. In a real medium, absorption and dispersive response may be related and the output bath may carry a correlated signal. The local Lindblad model assumes these complications can be neglected or separately calibrated. The explicit mechanical oscillator is now retained, with a known-frequency thermal bath, while the atoms remain stationary. There is no coherent optical drive, no optical multimode field, and no modulation of atomic couplings by displacement. The mechanical parameter sets are dimensionless theoretical choices, not fitted parameters of a realized device. Mechanical damping is described by the stated local Lindblad model. These restrictions and the phonon-convergence tests define the scope of the hybrid predictions.

9 Conclusions

We have extended atomic-only Kerr and loss estimation to two three-level atoms in an explicit optomechanical cavity. The unconditional dynamics retains nonlinear radiation pressure, optical and atomic loss, mechanical damping and heating, and parameter-independent thermal preparation. The ten-state optical sector remains exact, while the mechanical basis is separately converged. Nested QFIMs distinguish information accessible from the atoms from that retained in the cavity and mechanics.

At the tested operating point, mechanical coupling lowers the atomic effective Kerr information by approximately 25.0%, and thermal mechanical occupation produces further deterioration. Treating coupling as an additional unknown introduces a separate calibration cost. A square-completion identity identifies the induced Kerr contribution, while the comparison with a static surrogate shows why it cannot generally replace the full transient hybrid calculation. These results specify a parameter regime with mechanical sensitivity loss rather than a universal enhancement or suppression theorem.

The zero-time QFI remains exactly zero, and no number of mechanical phonons enables intrinsic-Kerr sensing with at most one optical or atomic excitation under this Hamiltonian. The resonance-sign symmetry, independently optimized qutrit–qubit gains, and simulated likelihood fits retained from the reference study are explicitly restricted to zero mechanical coupling. Future device-level work can test coupled-case control optimization, detector errors, nonlocal bath models, and the cost of calibrating mechanical parameters. The accompanying authors' working package retains numerical outputs and source programs for reproduction of the reported hybrid benchmarks.

Declarations

Funding. No external funding or financial support was received for this research.

Conflict of interest. The authors declare no competing financial or non-financial interests.

Author contributions. S. Jamal Anwar was responsible for conceptualization, methodology, theoretical modeling, software development, validation, formal analysis, numerical calculations, visualization, and preparation and revision of the manuscript. S. Abdul Khalek critically reviewed the manuscript. The stated roles reflect the author information supplied for this project.

Data availability. No experimental, observational, or third-party datasets were generated or analyzed. The reported results arise from theoretical calculations and numerical simulations. Supporting numerical arrays are retained in the accompanying authors' working package; no dataset has been deposited in a public repository.

Code availability. Custom Python and MATLAB/Octave scripts were used in the numerical calculations and checks. They are retained in the accompanying authors' working package but have not been deposited in a public repository.

Materials availability. Not applicable; no physical experimental materials were used.

Ethics approval. Not applicable; the study involved no human participants, animals, or identifiable personal data.

Consent to participate. Not applicable; there were no research participants.

Consent for publication. Not applicable to participant-related material; no identifiable personal information or case material is included.

A Resonant harmonic symmetry with cavity leakage

Set $\zeta = 0$ and $\delta = \eta = \gamma = 0$, retain real identical couplings, and take the initial state in Eq. (7). At $N = 2$, the dark atomic combination orthogonal to Eq. (20) is never populated. The independent mechanical state factors out. The bright-sector atom–field Hamiltonian is

$$\mathcal{H}_B(x) = \begin{pmatrix} 2x & 2 & 0 \\ 2 & 0 & \sqrt{2+r^2} \\ 0 & \sqrt{2+r^2} & 0 \end{pmatrix}, \quad \mathcal{H}_B(-x) = -P\mathcal{H}_B(x)P, \quad P = \mathrm{diag}(1,-1,1). \tag{31}$$

Complex conjugation combined with P maps the Schrödinger equation at x to that at $-x$. The cavity-loss no-jump term is diagonal and unchanged by this transformation. Cavity annihilation lowers photon occupation while preserving atomic excitation, so its action between excitation sectors commutes with the parity $(-1)^{N_{\mathrm{atoms}}}$ that defines the corresponding P matrices. Each trajectory probability is unchanged. Averaging all trajectories therefore preserves equality of the bright-sector atomic weights under $x \mapsto -x$.

At $N = 1$, Kerr vanishes and only the symmetric single-atomic-excitation state is populated by the exchange and cavity jumps. At $N = 0$, the state is $|00, 0\rangle$. Partial tracing the field

removes coherences between different atomic excitation numbers. The remaining atomic projectors are precisely those in Eq. (21), and their weights are even functions. This proves the atomic sign ambiguity for the stated preparation and channel. The proof does not impose a no-jump conditioning on the readout; it uses trajectories only as a representation of the complete master equation.

B Exchange norm in the accessible excitation sector

With the diagonal energies removed from Eq. (19), the symmetric two-excitation exchange matrix is a star graph centered on $|S_{01}, 1\rangle$, with couplings $(2, \sqrt{2}, r)g_0$. Its nonzero eigenvalues are

$$\lambda_\pm = \pm g_0\sqrt{4+2+r^2} = \pm g_0\sqrt{6+r^2}. \tag{32}$$

The antisymmetric two-excitation block has exchange norm $|r|g_0$, and the one-excitation bright block has norm $\sqrt{2}g_0$, both smaller than the symmetric value. For two qubits, the symmetric two-excitation chain has couplings $2g_q$ and $\sqrt{2}g_q$, giving norm $\sqrt{6}g_q$. Equality yields Eq. (22). This derivation concerns the interaction operator on $N \leq 2$; it does not equate the complete free-energy spectra of the two devices.

References

[1] S. L. Braunstein, C. M. Caves, Statistical distance and the geometry of quantum states, *Physical Review Letters 72, 3439-3443* (1994). 10.1103/physrevlett.72.3439.

[2] M. G. A. Paris, Quantum estimation for quantum technology, *International Journal of Quantum Information 07, 125-137* (2009). 10.1142/s0219749909004839.

[3] D. Petz, C. Ghinea, Introduction to quantum Fisher information, *Quantum Probability and Related Topics , 261-281* (2011). 10.1142/9789814338745_0015.

[4] A. Fujiwara, Quantum channel identification problem, *Physical Review A 63, 042304* (2001). 10.1103/physreva.63.042304.

[5] R. Demkowicz-Dobrzański, J. Kołodyński, M. Guţă, The elusive Heisenberg limit in quantum-enhanced metrology, *Nature Communications 3, 1063* (2012). 10.1038/ncomms2067.

[6] S. Alipour, M. Mehboudi, A. T. Rezakhani, Quantum Metrology in Open Systems: Dissipative Cramér-Rao Bound, *Physical Review Letters 112, 120405* (2014). 10.1103/physrevlett.112.120405.

[7] X. M. Lu, X. Wang, C. P. Sun, Quantum Fisher information flow and non-Markovian processes of open systems, *Physical Review A 82, 042103* (2010). 10.1103/physreva.82.042103.

[8] S. J. Anwar, M. Ramzan, M. K. Khan, Effect of Stark- and Kerr-like medium on the entanglement dynamics of two three-level atomic systems, *Quantum Information Processing 18, 192* (2019). 10.1007/s11128-019-2277-7.

[9] S. Abdel-Khalek, Quantum Fisher information for moving three-level atom, *Quantum Information Processing 12, 3761-3769* (2013). 10.1007/s11128-013-0622-9.

[10] S. Jamal Anwar, M. Ramzan, M. Usman, et al., Thermal and intrinsic decoherence effects on the dynamics of two three-level moving atomic system, *Physica A: Statistical Mechanics and its Applications 549, 124297* (2020). 10.1016/j.physa.2020.124297.

[11] S. J. Anwar, M. Ramzan, M. K. Khan, Quantum Fisher Information of Three-Level Atom under the Influence of the Stark Effect and Intrinsic Dechorence, *Atoms 11, 42* (2023). 10.3390/atoms11030042.

[12] S. J. Anwar, M. Ibrahim, M. K. Khan, et al., Quantum coherence in three-level systems under the combined effect of stark effect and non-linear Kerr medium, *Scientific Reports 16, 453* (2026). 10.1038/s41598-025-29866-7.

[13] H. R. Baghshahi, M. K. Tavassoly, Entanglement, quantum statistics and squeezing of twoΞ-type three-level atoms interacting nonlinearly with a single-mode field, *Physica Scripta 89, 075101* (2014). 10.1088/0031-8949/89/7/075101.

[14] H. R. Baghshahi, M. K. Tavassoly, Dynamics of different entanglement measures of two three-level atoms interacting nonlinearly with a single-mode field, *The European Physical Journal Plus 130, 37* (2015). 10.1140/epjp/i2015-15037-1.

[15] X. Zou, K. Pahlke, W. Mathis, Generation of an entangled state of two three-level atoms in cavity QED, *Physical Review A 67, 044301* (2003). 10.1103/physreva.67.044301.

[16] P. D. Drummond, D. F. Walls, Quantum theory of optical bistability. I. Nonlinear polarisability model, *Journal of Physics A: Mathematical and General 13, 725-741* (1980). 10.1088/0305-4470/13/2/034.

[17] B. Yurke, D. Stoler, Generating quantum mechanical superpositions of macroscopically distinguishable states via amplitude dispersion, *Physical Review Letters 57, 13-16* (1986). 10.1103/physrevlett.57.13.

[18] G. Kirchmair, B. Vlastakis, Z. Leghtas, et al., Observation of quantum state collapse and revival due to the single-photon Kerr effect, *Nature 495, 205-209* (2013). 10.1038/nature11902.

[19] B. Vlastakis, G. Kirchmair, Z. Leghtas, et al., Deterministically Encoding Quantum Information Using 100-Photon Schrödinger Cat States, *Science 342, 607-610* (2013). 10.1126/science.1243289.

[20] A. Monras, M. G. A. Paris, Optimal Quantum Estimation of Loss in Bosonic Channels, *Physical Review Letters 98, 160401* (2007). 10.1103/physrevlett.98.160401.

[21] M. A. C. Rossi, F. Albarelli, M. G. A. Paris, Enhanced estimation of loss in the presence of Kerr nonlinearity, *Physical Review A 93, 053805* (2016). 10.1103/physreva.93.053805.

[22] M. Asjad, B. Teklu, M. G. A. Paris, Joint quantum estimation of loss and nonlinearity in driven-dissipative Kerr resonators, *Physical Review Research 5, 013185* (2023). 10.1103/physrevresearch.5.013185.

[23] M. N. Notarnicola, S. Olivares, M. G. A. Paris, Joint estimation of noise and nonlinearity in Kerr systems, *APL Quantum 1, 036118* (2024). 10.1063/5.0225120.

[24] R. Di Candia, F. Minganti, K. V. Petrovnin, et al., Critical parametric quantum sensing, *npj Quantum Information 9, 23* (2023). 10.1038/s41534-023-00690-z.

[25] N. Zidan, H. F. Abdel-Hameed, N. Metwally, Quantum Fisher information of atomic system interacting with a single cavity mode in the presence of Kerr medium, *Scientific Reports 9, 2699* (2019). 10.1038/s41598-019-39183-5.

[26] M. Aspelmeyer, T. J. Kippenberg, F. Marquardt, Cavity optomechanics, *Reviews of Modern Physics 86, 1391-1452* (2014). 10.1103/revmodphys.86.1391.

[27] P. Rabl, Photon Blockade Effect in Optomechanical Systems, *Physical Review Letters 107, 063601* (2011). 10.1103/physrevlett.107.063601.

[28] S. Aldana, C. Bruder, A. Nunnenkamp, Equivalence between an optomechanical system and a Kerr medium, *Physical Review A 88, 043826* (2013). 10.1103/physreva.88.043826.

[29] F. Schneiter, S. Qvarfort, A. Serafini, et al., Optimal estimation with quantum optomechanical systems in the nonlinear regime, *Physical Review A 101, 033834* (2020). 10.1103/physreva.101.033834.

[30] V. Montenegro, M. G. Genoni, A. Bayat, et al., Probing of nonlinear hybrid optomechanical systems via partial accessibility, *Physical Review Research 4, 033036* (2022). 10.1103/physrevresearch.4.033036.

[31] F. Daneshmand, H. R. Baghshahi, S. Yahya Mirafzali, Quantum Fisher information of a diamond-type four-level atom interacting with a single-mode quantized field in an optomechanical cavity, *Communications in Theoretical Physics 77, 045105* (2025). 10.1088/1572-9494/ad9257.

[32] K. Matsumoto, A new approach to the Cramér-Rao-type bound of the pure-state model, *Journal of Physics A: Mathematical and General 35, 3111-3123* (2002). 10.1088/0305-4470/35/13/307.

[33] S. Ragy, M. Jarzyna, R. Demkowicz-Dobrzański, Compatibility in multiparameter quantum metrology, *Physical Review A 94, 052108* (2016). 10.1103/physreva.94.052108.

[34] M. Szczykulska, T. Baumgratz, A. Datta, Multi-parameter quantum metrology, *Advances in Physics: X 1, 621-639* (2016). 10.1080/23746149.2016.1230476.

[35] F. Albarelli, J. F. Friel, A. Datta, Evaluating the Holevo Cramér-Rao Bound for Multiparameter Quantum Metrology, *Physical Review Letters 123, 200503* (2019). 10.1103/physrevlett.123.200503.

[36] J. S. Sidhu, Y. Ouyang, E. T. Campbell, et al., Tight Bounds on the Simultaneous Estimation of Incompatible Parameters, *Physical Review X 11, 011028* (2021). 10.1103/physrevx.11.011028.

[37] J. Suzuki, Explicit formula for the Holevo bound for two-parameter qubit-state estimation problem, *Journal of Mathematical Physics 57, 042201* (2016). 10.1063/1.4945086.

[38] S. Razavian, M. G. A. Paris, M. G. Genoni, On the Quantumness of Multiparameter Estimation Problems for Qubit Systems, *Entropy 22, 1197* (2020). 10.3390/e22111197.

[39] J. Suzuki, Y. Yang, M. Hayashi, Quantum state estimation with nuisance parameters, *Journal of Physics A: Mathematical and Theoretical 53, 453001* (2020). 10.1088/1751-8121/ab8b78.

[40] M. Tsang, F. Albarelli, A. Datta, Quantum Semiparametric Estimation, *Physical Review X 10, 031023* (2020). 10.1103/physrevx.10.031023.

[41] M. Tavis, F. W. Cummings, Exact Solution for an N -Molecule—Radiation-Field Hamiltonian, *Physical Review 170, 379-384* (1968). 10.1103/physrev.170.379.

[42] E. Jaynes, F. Cummings, Comparison of quantum and semiclassical radiation theories with application to the beam maser, *Proceedings of the IEEE 51, 89-109* (1963). 10.1109/proc.1963.1664.

[43] J. Koch, T. M. Yu, J. Gambetta, et al., Charge-insensitive qubit design derived from the Cooper pair box, *Physical Review A 76, 042319* (2007). 10.1103/physreva.76.042319.

[44] A. Blais, R. S. Huang, A. Wallraff, et al., Cavity quantum electrodynamics for superconducting electrical circuits: An architecture for quantum computation, *Physical Review A 69, 062320* (2004). 10.1103/physreva.69.062320.

[45] A. Blais, A. L. Grimsmo, S. M. Girvin, et al., Circuit quantum electrodynamics, *Reviews of Modern Physics 93, 025005* (2021). 10.1103/revmodphys.93.025005.

[46] A. Wallraff, D. I. Schuster, A. Blais, et al., Strong coupling of a single photon to a superconducting qubit using circuit quantum electrodynamics, *Nature 431, 162-167* (2004). 10.1038/nature02851.

[47] D. I. Schuster, A. A. Houck, J. A. Schreier, et al., Resolving photon number states in a superconducting circuit, *Nature 445, 515-518* (2007). 10.1038/nature05461.

[48] J. M. Fink, M. Göppl, M. Baur, et al., Climbing the Jaynes–Cummings ladder and observing its nonlinearity in a cavity QED system, *Nature 454, 315-318* (2008). 10.1038/nature07112.

[49] A. Reiserer, G. Rempe, Cavity-based quantum networks with single atoms and optical photons, *Reviews of Modern Physics 87, 1379-1418* (2015). 10.1103/revmodphys.87.1379.

[50] M. Hofheinz, E. M. Weig, M. Ansmann, et al., Generation of Fock states in a superconducting quantum circuit, *Nature 454, 310-314* (2008). 10.1038/nature07136.

[51] M. Hofheinz, H. Wang, M. Ansmann, et al., Synthesizing arbitrary quantum states in a superconducting resonator, *Nature 459, 546-549* (2009). 10.1038/nature08005.

[52] B. Mischuck, K. Mølmer, Qudit quantum computation in the Jaynes-Cummings model, *Physical Review A 87, 022341* (2013). 10.1103/physreva.87.022341.

[53] B. P. Lanyon, M. Barbieri, M. P. Almeida, et al., Simplifying quantum logic using higher-dimensional Hilbert spaces, *Nature Physics 5, 134-140* (2009). 10.1038/nphys1150.

[54] R. Bianchetti, S. Filipp, M. Baur, et al., Control and Tomography of a Three Level Superconducting Artificial Atom, *Physical Review Letters 105, 223601* (2010). 10.1103/physrevlett.105.223601.

[55] W. K. Wootters, B. D. Fields, Optimal state-determination by mutually unbiased measurements, *Annals of Physics 191, 363-381* (1989). 10.1016/0003-4916(89)90322-9.

[56] I. D. Ivonovic, Geometrical description of quantal state determination, *Journal of Physics A: Mathematical and General 14, 3241-3245* (1981). 10.1088/0305-4470/14/12/019.

[57] D. F. V. James, P. G. Kwiat, W. J. Munro, et al., Measurement of qubits, *Physical Review A 64, 052312* (2001). 10.1103/physreva.64.052312.

[58] Z. Hradil, Quantum-state estimation, *Physical Review A 55, R1561-R1564* (1997). 10.1103/physreva.55.r1561.

[59] R. D. Gill, S. Massar, State estimation for large ensembles, *Physical Review A 61, 042312* (2000). 10.1103/physreva.61.042312.

[60] M. G. Genoni, Cramér-Rao bound for time-continuous measurements in linear Gaussian quantum systems, *Physical Review A 95, 012116* (2017). 10.1103/physreva.95.012116. Erratum: *Physical Review A 95*, 059908 (2017), 10.1103/PhysRevA.95.059908.

[61] G. Lindblad, On the generators of quantum dynamical semigroups, *Communications in Mathematical Physics 48, 119-130* (1976). 10.1007/bf01608499.

[62] V. Gorini, A. Kossakowski, E. C. G. Sudarshan, Completely positive dynamical semigroups of N -level systems, *Journal of Mathematical Physics 17, 821-825* (1976). 10.1063/1.522979.

[63] E. B. Davies, Markovian master equations, *Communications in Mathematical Physics 39, 91-110* (1974). 10.1007/bf01608389.

[64] C. W. Gardiner, M. J. Collett, Input and output in damped quantum systems: Quantum stochastic differential equations and the master equation, *Physical Review A 31, 3761-3774* (1985). 10.1103/physreva.31.3761.

[65] M. B. Plenio, P. L. Knight, The quantum-jump approach to dissipative dynamics in quantum optics, *Reviews of Modern Physics 70, 101-144* (1998). 10.1103/revmodphys.70.101.

[66] J. Dalibard, Y. Castin, K. Mølmer, Wave-function approach to dissipative processes in quantum optics, *Physical Review Letters 68, 580-583* (1992). 10.1103/physrevlett.68.580.

[67] H. Carmichael, An Open Systems Approach to Quantum Optics, *Lecture Notes in Physics Monographs* (1993). 10.1007/978-3-540-47620-7.

[68] D. Hu, S. Y. Huang, J. Q. Liao, et al., Quantum coherence in ultrastrong optomechanics, *Physical Review A 91, 013812* (2015). 10.1103/physreva.91.013812.

[69] M. T. Naseem, A. Xuereb, Ö. E. Müstecaplıoğlu, Thermodynamic consistency of the optomechanical master equation, *Physical Review A 98, 052123* (2018). 10.1103/physreva.98.052123.

[70] D. Šafránek, Discontinuities of the quantum Fisher information and the Bures metric, *Physical Review A 95, 052320* (2017). 10.1103/physreva.95.052320.